

Chapter 12

Corrosion in Complex Environments

12.1 INTRODUCTION

The high-temperature corrosion processes considered so far lead to the formation of solid reaction products, and their kinetics are in most cases controlled by solid-state diffusion. However, gaseous and liquid corrosion products are also possible. Because mass transport in liquids is so much faster than in solids, and in the gas phase faster still, the rate of material loss is greatly accelerated and can be catastrophic. Many examples of this type of corrosion are to be found in combustion processes, which form the focus of this chapter.

Combustion generates rather complex reaction products, which vary considerably with the nature of the fuel. Even conventional coal combustion leads to flue gas containing SO_x , and sometimes chloride species, as well as CO_2 and H_2O , and ashes which can contain aggressive species. A number of new and prospective technologies present more chemically complex environments which challenge the conventional materials selection process. For example, a desire to utilise waste streams rather than simply disposing of them as landfill leads to processes such as municipal waste combustion to generate power and/or provide district heating. Unfortunately, burning municipal waste produces much more aggressive environments than fossil fuel combustion, as the waste typically contains significant amounts of PVC plastic, as well as surprising levels of a diversity of metals.

Somewhat similar environments can result from the use of biomass in firing boilers for power generation. Flue gases containing significant levels of HCl and large quantities of ash are produced. Examples of combustion gas [1,2] and ash analyses [3–7] are shown in Tables 12.1 and 12.2. Some ashes fuse at operating temperatures, and the effect of the resulting liquid phases on corrosion must be considered.

Corrosion environments can also be made complex by contamination. The operation of turbines or other combustion equipment in locations where the air is severely polluted, or in marine environments where salt spray is frequent, provides common examples.

TABLE 12.1 Combustion Flue Gas Compositions (Vol. %)

Source	O ₂	CO ₂	SO ₂ (ppm)	HCl (ppm)	H ₂ O	References
Waste: Harrisburg, USA	9.0	7.5	135	485	8.8	[1]
Waste: Europe	5.7 –13	9.5 –13.9	38 –500	260 –690	n/a	[1]
Waste: Japan	7.8 –11.6	8.6 –12.3	0–65	422 –1300	16.6 –21	[1]
Waste: Japan	8.0 –9.0	10.5 –11.6	18–22	250 –330	16 –22	[2]

As seen in earlier chapters, the presence of a secondary corrodent (sulphur, carbon, etc.) in addition to oxygen can lead to the appearance of additional reaction product phases, either in the scale or precipitated within the alloy. Thermodynamic prediction of the range of possible outcomes is always possible, but prediction of the actual diffusion path adopted by the reaction system is usually not. This deficiency arises because knowledge of the mechanism whereby secondary reactants pass through the scale is so limited, and quantitative diffusion data is nonexistent. Since, moreover, halogens are able to form volatile compounds with many metals of interest, rather different corrosion mechanisms become possible. An example is seen in Fig. 12.1, which shows the result of exposing stainless steel 353 MA to a chloride melt. The porous residue had a composition of approximately 43Fe-56Ni-1Cr (wt%) compared to the original alloy of 36Fe-35Ni-26Cr, indicating substantial loss of chromium and some loss of iron.

12.2 VOLATILISATION BY HALOGENS

Fluorine and chlorine are quite abundant in nature, the former largely as the mineral fluorite, CaF₂, and the latter in ionic form in seawater. Both are used in the chemical industry, and chlorine is particularly important for its use in PVC. This commodity plastic is produced on a very large scale: 35 Mt in 2010, increasing at about 5% per annum [8]. High-temperature corrosion by fluorine is common in the aluminium industry, where molten cryolite, 3NaF·AlF₃, is used to dissolve alumina for electrolysis. Moisture in the feed materials reacts to form HF, which corrodes overhead structures above the smelting pots.

High-temperature chlorine corrosion is a more widespread problem, and examples of environments in which it occurs are given in Table 12.2. In the gas phase, the Deacon reaction

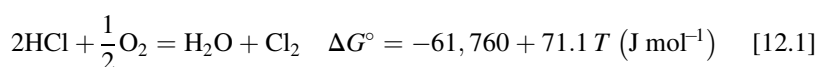


TABLE 12.2 Some Combustion Ash Deposit Compositions (Wt%)

Source	Al	Si	Fe	Na	K	Ca	Mg	Pb	Zn	S	Cl	H ₂ O	References
^a Waste — Tokyo	5.03	6.13	0.65	2.72	2.86	26.2	1.94	0.02	0.51	5.06	7.15	1.63	[7]
^a Waste —Japan	5.2	8.95	1.98	5.50	4.80	11.0		0.43	1.51	4.50	10.5		[6]
^b Waste — USA	P ^c	P ^c		1.2	2.9	P ^c		29.6	0.39	2.0	12.8		[3]
^b Biomass — straw		1.81	2.09		46.6	3.41				2.36	41.6		[4]
^a Biomass — straw	0.3–0.9	18–25			15–20	7.5–9				0.4–1.7	3–4		[5]

^aBalance oxygen.^bOxygen omitted.^cPresent.

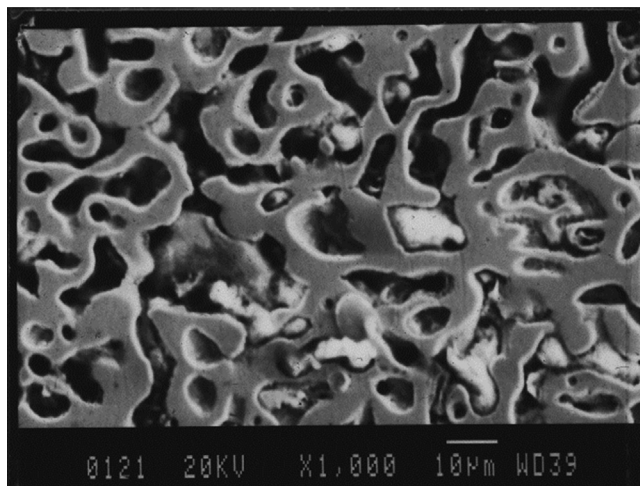


FIGURE 12.1 SEM image of section through alloy 353 MA after exposure to a $\text{BaCl}_2\text{-NaCl}$ melt at 1050°C for 45 days.

controls chlorine speciation in the absence of alkali metals, and the relative abundance of Cl_2 and HCl can vary greatly at intermediate temperatures. For example, the equilibrium constant $K_{12.1} = 0.6$ at 650°C . In moist air, with $p_{\text{O}_2} = 0.21$ atm and $p_{\text{H}_2\text{O}} = 0.01$ atm, then $p_{\text{Cl}_2}/p_{\text{HCl}}^2 = 12.6 \text{ atm}^{-1}$. In a combustion gas with $p_{\text{H}_2\text{O}} = 0.12$ and $p_{\text{O}_2} = 0.02$ atm, however, $p_{\text{Cl}_2}/p_{\text{HCl}}^2 = 0.01 \text{ atm}^{-1}$. It is for this reason that chlorine-bearing flue gases contain HCl (Table 12.2).

12.2.1 Corrosion by Chlorine

Metal chloride formation is seen in Table 12.3 to be favoured for common metals, although chlorides are considerably less stable than the corresponding oxides. Metal chloride melting points are low, and the vapour pressures of gas-phase species are high. Tabulated data [9] plotted in Fig. 12.2 shows some examples. As volatilisation rates in flowing gas streams are proportional to partial pressure (Eq. [2.157]), the rate of iron loss from a steel is expected to greatly exceed that of nickel or chromium.

Early work on corrosion in pure gaseous chlorine confirmed that metal loss by volatilisation is the dominant process for many metals. Chloridation of nickel is found [10] to follow a rate law corresponding to Eq. [1.36]

$$\frac{d\Delta W/A}{dt} = \frac{k_w}{\Delta W/A} - k_v \quad [12.2]$$

At low temperatures, k_v is negligible, and the kinetics are close to parabolic in the short-term. Parabolic kinetics of the form shown in Fig. 11.9 are in

TABLE 12.3 Metal Chloride-Free Energies of Formation and Melting Points [29]

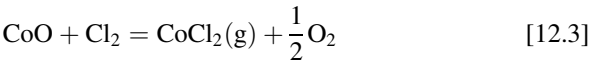
Chloride	$\Delta G_f^\circ = A + BT \text{ (J mol}^{-1}\text{)}$		MP (°C)
	A	B	
FeCl ₂ (s)	−356,423	116.3	673
FeCl ₂ (l)	−286,394	63.68	
NiCl ₂ (s)	−298,549	143.6	1001
CrCl ₂ (s)	−353,046	83.26	815
CrCl ₃ (s)	−532,372	208.5	1152
CrO ₂ Cl ₂ (g)	−538,100	122.4	−96.5
AlCl ₃ (g)	−581,182	52.14	190 (sublimes)
AlOCl(g)	−348,890	3.874	
TiCl ₄ (g)	−753,768	120.1	
PbCl ₂ (l)	−331,999	111.7	501
ZnCl ₂ (l)	−393,087	114.4	283

effect at temperatures of 430–525°C, and at higher temperatures the volatilisation term is dominant. Iron and low alloy steels react much faster [11], with volatilisation predominant. Of course, volatilisation losses depend on gas flow rates, as predicted by Eq. [2.158].

Early work by Tamman [12] on the halogenation of silver, copper and lead is of historic interest, as it provided some of the first demonstrations of parabolic kinetics. Volatilisation was avoided in these experiments, as temperatures were low, accounting for the simple kinetics observed.

12.2.2 Corrosion by Oxygen-Chlorine Mixtures

It is well-known [13–15] that chlorine accelerates the oxidation of metals and alloys, leading to linear reaction kinetics and the growth of porous oxide scales, followed by sustained weight loss. McNallan et al. [16,17] demonstrated that in the case of cobalt exposed to Ar-1% O₂-1% Cl₂ gases at 727°C, weight losses were due to volatilisation of CoCl₂



with the long-term weight loss occurring at a constant rate. This rate was shown to be proportional to the square root of gas flow velocity, in accord with Eq. [2.158] for gas-phase mass transfer.

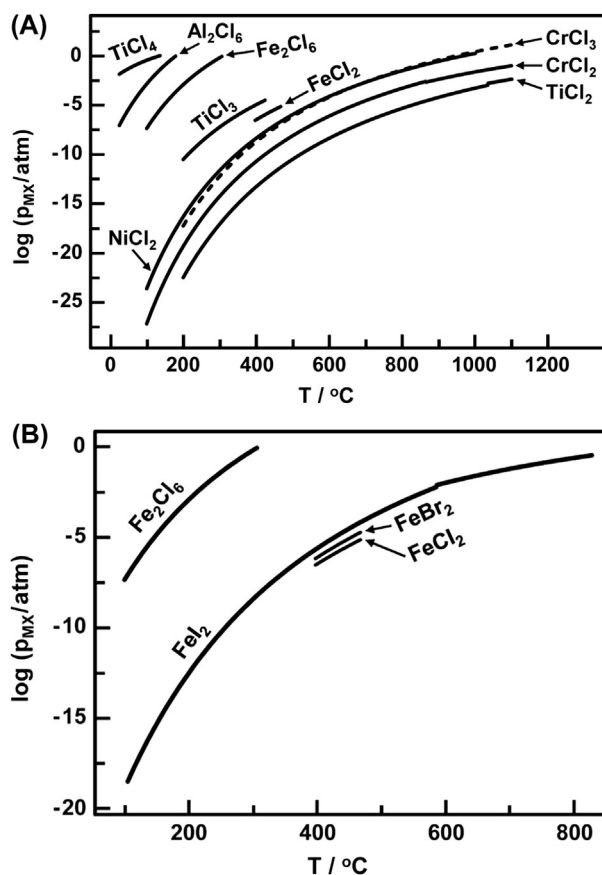


FIGURE 12.2 Vapour pressures of metal chlorides in equilibrium with unit activity condensed phases: (A) selected metal chlorides and (B) iron halides.

It is clearly important to know how rapidly metal is consumed when halide volatilisation is occurring. Latreche et al. [18,19] have extended conventional thermochemical diagrams (Section 2.2.2) to define gas-phase potentials corresponding to a particular partial pressure of the metal halide of interest. They considered two modes of volatilisation: into an extremely low pressure environment via the Hertz–Langmuir–Knudsen Eq. [2.155], and the more common situation of mass transfer into a flowing gas (Eq. [2.157]).

The remaining reaction product was porous oxide, containing very little chlorine. Reaction [12.3] is thermodynamically favoured only at low oxygen potentials, ie, within and beneath the oxide scale. At high oxygen potentials, the reverse of Eq. [12.3] is favoured, and oxide is deposited at or near the scale surface as a porous solid. This ‘active oxidation’ mechanism is shown schematically in Fig. 12.3, and the corresponding diffusion path is mapped in

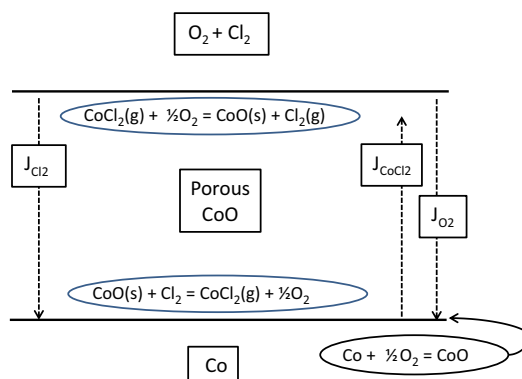


FIGURE 12.3 Schematic diagram of active oxidation mechanism for Co exposed to oxygen and chlorine.

Fig. 12.4. Reaction in a gas mixture of Ar-50% O_2 -1% Cl_2 led to linear weight uptake kinetics, corresponding to continuing oxide formation, volatilisation and redeposition.

Oh et al. [20] studied the reaction in Ar-20 O_2 -2 Cl_2 at 900°C of 310 stainless, alloy 800 and a series of nickel-base alloys. Alloy 800, 310 stainless and chromia-forming nickel-base alloys all suffered weight losses due to volatile chloride formation, whilst developing porous, nonprotective chromia scales and internal porosity. The internal attack was suggested to be due to chromium chloride formation, consistent with the greater stability of the latter, compared with that of iron or nickel chlorides (Table 12.3). Moreover, chlorine permeabilities in nickel are relatively high, as shown by Li and Rapp [21] in a study of internal chloridation of dilute Ni-Cr alloys exposed to a Ni/ $NiCl_2$ Rhines pack. The higher chromium levels of the alloys corroded by Oh et al. [20]

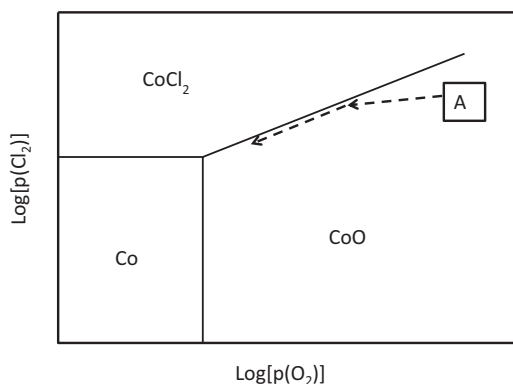
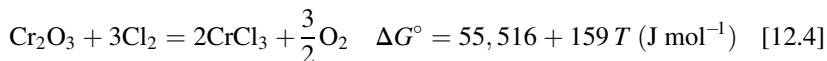


FIGURE 12.4 Thermochemical diagram for Co- O_2 - Cl_2 , showing diffusion path for active oxidation mechanism.

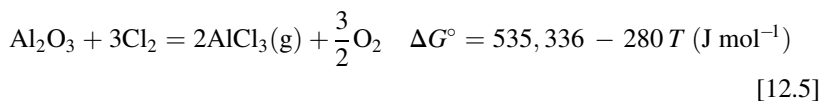
would have led to much higher precipitate volume fractions, and perhaps a degree of continuity which allowed volatilisation of either CrO_2Cl_2 or the chloride itself.

The poor performance of chromia-forming alloys is of interest, as the volatility of the chromium chlorides is not particularly high (Fig. 12.2), and the reaction

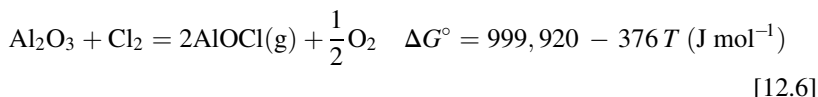


is not favoured in oxidising atmospheres. The explanation lies in the formation of CrO_2Cl_2 , shown by Ebbinghaus [22] to be the predominant vapour species in the Cr-O-Cl system over a wide range of temperatures. Solid Cr_2O_3 in equilibrium with 0.1 atm O_2 and 0.01 atm Cl_2 at temperatures of 500–1000°C produces oxychloride vapour at a pressure of about 10^{-6} atm [22].

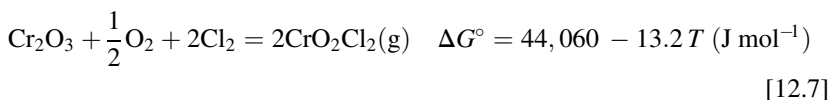
Of the alloys studied by Oh et al. [20], only the alumina-forming alloy 214 displayed resistance to attack by the oxygen-chlorine gas, forming a protective scale of alumina. An important factor in the resistance of alumina to chloridation is the stability of the oxide. Using data from Tables 2.1 and 12.3, one writes



Pure solid alumina in equilibrium with $p_{\text{O}_2} = 0.2$ atm and $p_{\text{Cl}_2} = 0.01$ atm at 900°C generates $p_{\text{AlCl}_3} = 7 \times 10^{-15}$ atm, a value too low for significant volatilisation. Considering oxychloride formation



compared with



it is calculated that for pure solid oxides in equilibrium at 900°C with $p_{\text{O}_2} = 0.2$ atm and $p_{\text{Cl}_2} = 0.01$ atm, $p_{\text{AlOCl}} = 5 \times 10^{-14}$ atm, whereas $p_{\text{CrO}_2\text{Cl}_2} = 1 \times 10^{-3}$ atm. Thus both the stability of alumina scales and the failure of chromia when exposed to these conditions are explained.

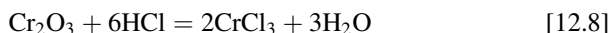
Alumina scales must also act as barriers to chlorine penetration. At the alumina scale-alloy interface, p_{O_2} is set by the $\text{Al}/\text{Al}_2\text{O}_3$ equilibrium at a very low value. At 900°C, if a_{Al} in the alloy is 0.1, then the interfacial value of p_{O_2} is 2×10^{-36} atm, and AlCl_3 formation via Eq. [12.5] requires only a very low chlorine potential. A value of $p_{\text{AlCl}_3} = 1$ atm would be produced if p_{Cl_2} reached the level of only 2×10^{-15} atm. It is therefore concluded that alumina scales are essentially impervious to chlorine.

At lower temperatures, the development of a protective alumina scale on commercial alloys is more difficult, simply because alloy diffusion is slow. Thus alloy 214 exposed to dry air +2%Cl₂ at temperatures of 500–800°C underwent active oxidation in the absence of a continuous alumina scale layer [23]. In contrast, Fe₃Al was able to form a protective Al₂O₃ layer at the base of its scale and underwent no chlorine attack.

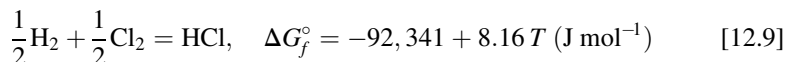
12.2.3 Corrosion by HCl

Pure metals iron [24], nickel [25] and chromium [26] react with pure HCl(g) at temperatures of 400–800°C to form metal chlorides. As solids, they form scales whilst simultaneously vaporising at their outer surfaces, and the kinetics of Eq. [12.2] are observed. At low enough temperatures, where metal chloride partial pressures are low, scale thickening according to parabolic kinetics is predominant in the short-term. At higher temperatures, the scale reaches a steady-state thickness and linear weight loss kinetics are subsequently observed. In the case of iron, the observed reaction product, FeCl₂, melts at 673°C, and kinetics at higher temperatures are irregular and weight loss is rapid.

Although corrosion of bare metals in pure HCl is rapid, preoxidised metals are much more resistant. Bramhoff et al. [27] oxidised an Fe-20Cr alloy, producing a chromia scale, then exposed it to an HCl + H₂O mixture at 900°C. No porosity developed in the oxide. Abels and Strehblow [28] showed that preoxidised IN600 exposed at 700°C to HCl (in the absence of oxygen) resisted penetration of its chromia scale by chlorine. These observations reflect in part the stability of Cr₂O₃ with respect to chloridation. This reaction can be written



Using data from Tables 2.1 and 12.3, together with the reaction [29]



it is found that

$$\Delta G_{12.8}^\circ = -129,758 + 372.4 T \text{ (J mol}^{-1}\text{)} \quad [12.10]$$

At 650°C then, $K_{12.8} = 7.8 \times 10^{-13}$, and at equilibrium, $p_{\text{H}_2\text{O}}/p_{\text{HCl}}^2 = 9 \times 10^{-5}$, implying that very high HCl partial pressures would be required to cause reaction at normal humidity levels.

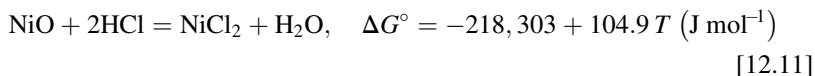
Although HCl does not penetrate a chromia scale, molecular chlorine does. Preoxidised IN600 subsequently exposed at 700°C to Ar-0.1%Cl₂ developed chlorine enrichment at its oxide-alloy interface, whilst simultaneously, iron appeared at the scale surface and iron chloride was found condensed downstream in the reactor [28]. The same results were observed for preoxidised

IN600 subsequently exposed to HCl plus O₂, as would be expected from reaction [12.1]. The mechanism whereby chlorine penetrates a chromia scale is not apparent, but once it does so, active oxidation (Fig. 12.3) accounts for the onset of the reaction with iron, leading to precipitation of iron oxide near the scale surface, and the loss of some FeCl₂ into the gas stream.

12.2.4 Corrosion by HCl Plus Oxygen

Early investigations by Ihara et al. into the corrosion by HCl + O₂ mixtures of iron [24], nickel [25] and chromium [26] revealed a seemingly complex pattern of behaviour. Corrosion of iron led to iron oxide formation and faster rates of metal consumption than in reaction with HCl alone. The corrosion of nickel in HCl + O₂ produced no oxide, and metal consumption was at the same rate as in pure HCl. Chromium grew an oxide scale in the gas mixtures, which provided protection against volatilisation up to temperatures of about 500°C, but oxidation was accompanied by accelerated weight losses at higher temperatures. These divergent results reflect simply the different reaction products.

Iron forms an oxide scale in HCl + O₂ but is subject to active oxidation. Because the chlorine activity is much higher in the gas mixture than in pure HCl (see Eq. [12.1]), the reaction product FeCl₃ is stabilised. As seen in Fig. 12.2, this substance has an extremely high vapour pressure, and volatilisation rates are accordingly rapid. In contrast, nickel cannot form an oxide in these gas mixtures. The reaction



strongly favours chloride formation, with a value of $K_{12.11} = 4 \times 10^7$ at 600°C. No higher chloride of nickel exists, and volatilisation rates are therefore unaffected by the presence of oxygen.

Chromium forms quite a stable oxide, which appears to resist chlorine attack at low temperatures. However, highly volatile oxychloride formation via reaction [12.6] is increasingly favoured at higher temperatures, and catastrophic rates of attack result.

Zahs et al. [30] examined the corrosion of these metals at much higher $p_{\text{O}_2}/p_{\text{Cl}_2}$ ratios, where the metal oxide was stable in contact with the gas. Active oxidation (Fig. 12.3) was observed for all three metals, as NiO was formed at the higher oxygen potential. Ferritic Fe-15Cr and Fe-35Cr alloys also underwent active oxidation at temperatures of 400–700°C. Net weight changes for these alloys are compared with those of several austenitic chromia-forming alloys in Fig. 12.5. The apparently better performance of the nickel-bearing alloys is illusory. The measured weight gains were less than the weight of oxygen in the scales, showing that metal had been lost from each

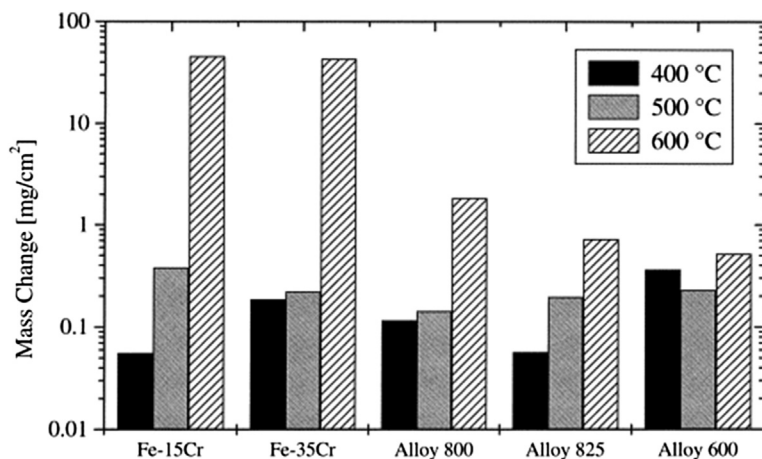


FIGURE 12.5 Mass changes after 168 h exposure in N_2 -5 vol% O_2 -1500 vppm HCl. Reprinted from A. Zahs, M. Spiegel, H.J. Grabke, *Corros. Sci.* 42 (2000) 1093, with permission from Elsevier.

alloy. The reason for this is the high stability of $NiCl_2$ with respect to the oxide (Eq. [12.11]), which allows some of the chloride vapour to escape from the scale before oxidation. Cross-sections of reacted alloys in Fig. 12.6 show the porous oxide scales resulting from the active oxidation mechanism, together with selective attack of the more reactive metals in the sub-surface alloy regions.

The marginal chromia former, IN600, is strongly attacked in O_2 /HCl mixtures at 700°C [28]. Analysis of scale compositions by XPS shows in Fig. 12.7 that chlorine did not enter the scale in the very early stages of reaction, being found only at the chromia-scale surface. However, after 100 min of reaction, chlorine penetrated the scale and attacked the underlying alloy.

A series of chromia-forming nickel-base alloys exposed at 900°C to Ar -5.5% O_2 -0.96% HCl -0.86% SO_2 underwent significant internal attack, developing internal voids beneath a chromia scale and volatilising metal chlorides or oxychlorides [31]. On the other hand, alloy 214 was effectively protected by its alumina scale, leading to the conclusion [31] that diffusion of chlorine species through Cr_2O_3 scales is faster than through Al_2O_3 .

The greater permeability of chromia scales to chlorine might in principle be due to porosity developed as a result of oxychloride volatilisation, to which Cr_2O_3 is much more susceptible than Al_2O_3 . However, CrO_2Cl_2 formation is not a necessary condition for chlorine permeation of the scale, as shown by the experiments of Stott et al. [32], using a gas mixture of Ar -25% H_2 -10% HCl -5% CO -1% CO_2 . At 900°C, this gas is oxidising to aluminium and chromium, but not nickel, so scales of either pure chromia or alumina were grown on nickel- or iron-base alloys. At the low oxygen potential of this gas, oxychloride formation was negligible. Nevertheless, a chlorine species penetrated the chromia

scales, leading to base metal volatilisation. Where an alumina scale was formed, chlorine attack was largely suppressed. It is therefore concluded that the superiority of alumina over chromia in excluding chlorine is an intrinsic property of the oxide scale.

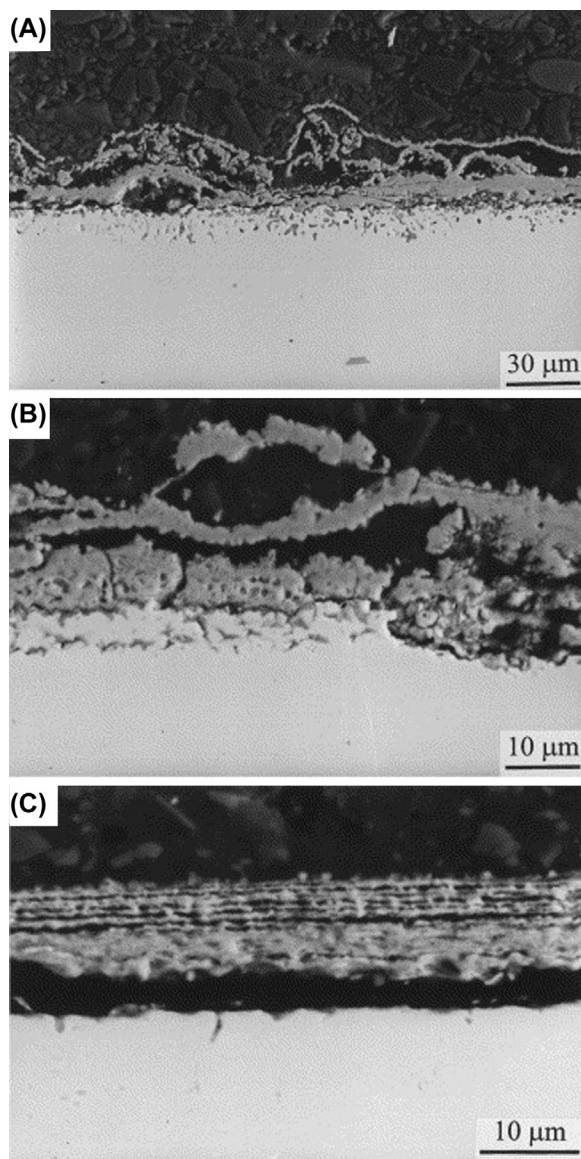


FIGURE 12.6 SEM images of cross-sections of nickel-containing alloys after 168 h exposure in N_2 -5 vol% O_2 -1500 vppm HCl at 600°C: (A) Alloy 800, (B) Alloy 825, (C) Alloy 600. Reprinted from A. Zahs, M. Spiegel, H.J. Grabke, *Corros. Sci.* 42 (2000) 1093, with permission from Elsevier.

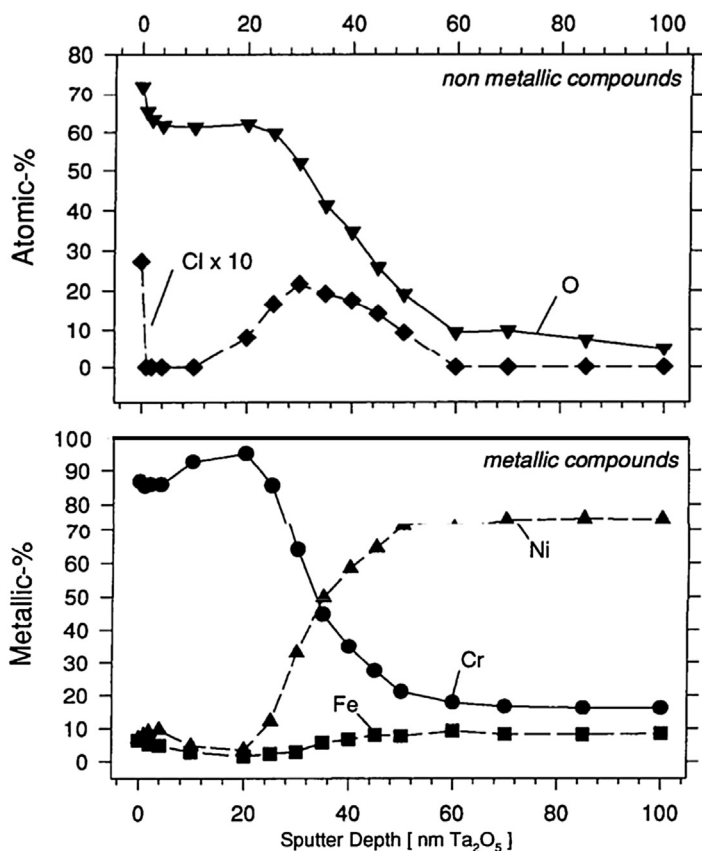


FIGURE 12.7 XPS sputter depth profile through scale on IN600 after 10 min exposure at 700°C to Ar-10%O₂-0.05%HCl. Reprinted from J.-M. Abels, H.-H. Strehblow, *Corros. Sci.* 39 (1996) 115 with permission from Elsevier.

12.2.5 Corrosion by HCl Plus Water Vapour

As noted in [Section 12.2.3](#), whereas chlorine penetrates chromia scales, HCl does not. A similar finding has been reached for iron oxide scales exposed to HCl-H₂O-O₂-N₂ gas mixtures [33]. This is at first sight puzzling, as these gas mixtures can yield relatively high chlorine partial pressures through reaction [12.1]. However, the environment which needs to be considered is that within the scale, where oxygen activities are low.

Iron exposed to N₂-50O₂-2.8H₂O-2.5HCl at 900°C grows a three-layered scale consisting mainly of FeO, with outer layers of Fe₃O₄ and Fe₂O₃, following parabolic kinetics at a rate close to that of iron in oxygen [33]. Rate data for a number of gas mixtures are compared in [Fig. 12.8](#), where the presence of HCl at levels ranging from 4×10^{-4} to 2.5% is seen to have little

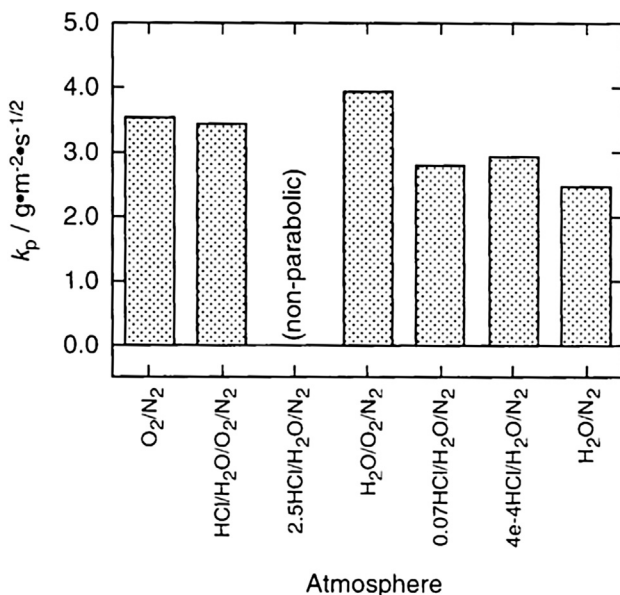


FIGURE 12.8 Parabolic weight change rates for pure iron in various gas mixtures at 900°C. Reprinted from Y. Sato, D.J. Young, in: T. Narita, T. Maruyama, S. Taneguchi (Eds.), *High Temperature Corrosion and Protection 2000*, Science Reviews, Northwood (2000) 119 with permission from Science Reviews.

effect in the presence of both oxygen and water vapour [34]. However, a mixture of N_2 -2.8 H_2O -2.5 HCl volatilised iron chloride, causing linear weight loss kinetics. These results are broadly understandable in simple thermodynamic terms.

Calculation of the gas-phase equilibria yields the p_{Cl_2} and p_{O_2} values plotted in the thermochemical diagram of Fig. 12.9. Most gases stabilise Fe_2O_3 , accounting for the growth of oxide scales, and the observed similarity in rates which are largely governed by the wüstite layer growth (Section 3.7.3). Conversely, the $\text{HCl}/\text{H}_2\text{O}/\text{N}_2$ gas is clearly in the $\text{FeCl}_2(\text{l})$ phase field, accounting for the observed volatilisation. Of more interest is the N_2 -50 O_2 -2.8 H_2O -2.5 HCl gas, which is calculated to yield an equilibrium value of $p_{\text{Cl}_2} = 2 \times 10^{-3}$ atm. This identifies the scale-gas composition point plotted in Fig. 12.9 as being on the $\text{FeCl}_2(\text{l})/\text{Fe}_2\text{O}_3$ phase boundary, and the diffusion path between this point and the underlying metal is critical to the reaction outcome.

If a chlorine species enters an iron oxide scale, oxidant potentials can be related by reaction [12.1], using the known p_{O_2} values at the three-phase boundaries Fe/FeO , $\text{FeO}/\text{Fe}_3\text{O}_4$ and $\text{Fe}_3\text{O}_4/\text{Fe}_2\text{O}_3$. To explore the consequences of HCl entry, it is assumed that p_{HCl} has its gas-phase value within the scale. If, furthermore, no H_2O enters the scale and therefore $p_{\text{Cl}_2} = p_{\text{H}_2\text{O}}$

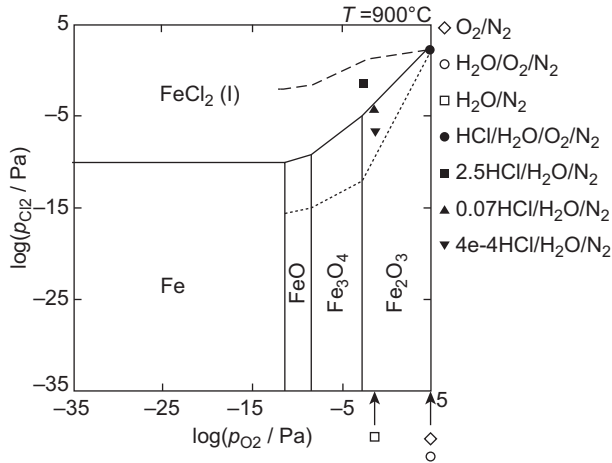


FIGURE 12.9 Thermochemical diagram for Fe-O-Cl at 900°C, showing gas compositions and possible diffusion paths for reaction with gas N_2 -50 O_2 -2.8 H_2O -2.5 HCl . Dashed line is diffusion path calculated for HCl entry into scale; dotted line approximates to actual observed diffusion path. Reprinted from Y. Sato, D.J. Young, in: T. Narita, T. Maruyama, S. Taneguchi (Eds.), *High Temperature Corrosion and Protection 2000, Science Reviews, Northwood (2000)* 119 with permission from Science Reviews.

according to the stoichiometry of Eq. [12.1], then p_{Cl_2} values for the three-phase boundaries can be calculated as

$$\frac{p_{Cl_2}^2}{p_{HCl}^2} = K_{12.1} p_{O_2}^{1/2} \quad [12.12]$$

The results define the diffusion path plotted in Fig. 12.9 for the 2.5% HCl gas mixture. It is seen that even under the supposition of rapid HCl diffusion, the chlorine potential decreases with depth in the oxide scale because p_{O_2} decreases markedly. Nonetheless, iron chloride is predicted to form under these conditions because local equilibrium values of p_{Cl_2}/p_{O_2} increase with depth. However, the prediction fails, as in fact an iron oxide scale develops, and the actual diffusion path is shown schematically in the figure.

Clearly, one or more of the assumptions underlying Eq. [12.12] is incorrect. If water vapour does enter the scale from the gas, then through reaction [12.1], it decreases the amount of Cl_2 formed. The size of this effect depends greatly on the effective fugacities of HCl and H_2O within the scale:

$$p_{Cl_2} = \frac{p_{HCl}^2}{p_{H_2O}} K_{12.1} p_{O_2}^{1/2} \quad [12.13]$$

Assuming as before that the gas-phase value applies for HCl within the scale, and making the same assumption for water vapour, then p_{Cl_2} values are depressed as shown in Table 12.4. Whilst the changes are significant, the

TABLE 12.4 Calculated Equilibrium Values of p_{Cl_2} (atm) Within Iron Oxide Scale in Contact With $\text{N}_2\text{-}50\text{O}_2\text{-}2.8\text{H}_2\text{O-}2.5\text{HCl}$ Gas at 900°C

Interface	Assumption re H_2O uptake	
	$p_{\text{Cl}_2} = p_{\text{H}_2\text{O}}$	$p_{\text{H}_2\text{O}} = 0.028 \text{ atm}$
Fe/FeO	5.6×10^{-7}	1.1×10^{-11}
FeO/Fe ₃ O ₄	1.8×10^{-6}	1.2×10^{-10}
Fe ₃ O ₄ /Fe ₂ O ₃	1.1×10^{-4}	3.6×10^{-7}

calculated compositions remain within the $\text{FeCl}_2(\text{l})$ phase field and are thus at variance with experimental observation. It must therefore be concluded that HCl has much lower potentials within the oxide scale, leading to lower chlorine potentials and oxide stability. Clearly, the presence of water vapour is important, as is its ability to enter oxide scales.

A comparison [35] between the behaviour of alloy 800 exposed to moist air (1.3% H_2O) and to the same atmosphere with 500 ppm HCl added showed that the presence of HCl promoted chromia-scale spallation on cooling from reaction temperature. This is consistent with enrichment of a chlorine species at the scale-alloy interface, leading to a loss of scale adhesion. However, if the alloy was preoxidised in moist air and then exposed to the HCl-containing moist air, no spallation occurred. Evidently water vapour already present in this chromia scale can exclude chlorine species, but fails to do so (at least at this low level) if the chlorine is present from the beginning of scale growth. Studies of the initial stages of reaction could reveal the mechanism of this effect.

12.3 CORROSION BY FLUE GASES AND SOLID CHLORIDES

Simulated flue gases are considered first. The corrosion of various alloys in gas mixtures containing low levels of HCl and SO_2 has been studied over a range of temperatures. Prescott et al. [31] exposed several nickel- and iron-base heat-resisting alloys to $\text{Ar-}5.5\text{O}_2\text{-}0.96\text{HCl-}0.86\text{SO}_2$ at 900°C , finding that volatilisation occurred in all cases, and that internal attack was always more extensive than the loss of metal section. The SO_2 was inactive under the conditions used. Void formation in alloy subsurface zones was common, reflecting loss of metal via chloride volatilisation. This form of attack was concentrated at grain boundaries, an effect attributed in part [36] to preferential attack on grain boundary carbides.

All chromia-forming alloys were attacked to various degrees. Only the alumina-forming alloy 214 developed a successful scale, one of $\alpha\text{-Al}_2\text{O}_3$. As

noted in Section 12.2.2, alumina is resistant to both chloridation and oxy-chloridation, as well as providing an effective barrier to chlorine ingress.

Less aggressive, but more realistic conditions were investigated by Sanchez Pasten and Spiegel [37]: a gas of $\text{N}_2\text{-8O}_2\text{-15H}_2\text{O}$ containing 2000 ppm HCl plus 200 ppm SO_2 at temperatures of 400–600°C. Alloy weight losses after 300 h of reaction are compared in Fig. 12.10. The superiority of nickel and the nickel-base alloy 625 over the different ferritic materials is due to the decreased volatility of NiCl_2 (Fig. 12.2A), whilst the failure of 22% of chromium in alloy 625 to provide any additional protection can be attributed to CrO_2Cl_2 volatilisation.

Exposure tests in gases containing oxygen and water vapour contaminated with HCl and SO_2 can provide insight into aspects of the corrosion mechanism but are unrealistic as a basis for understanding real flue gas corrosion. One obvious deficiency is the absence of potassium, an important participant in gas-phase reactions at high temperatures.

Thermodynamic calculation can be used to predict equilibrium compositions of flue gases resulting from the combustion of different fuels and to explore their variation with temperature. Results obtained for fluidised bed combustion of straw [5] are shown in Fig. 12.11, where KCl(g) is seen to become predominant above $T \sim 650^\circ\text{C}$. Although flue gases are at high temperatures, they contact heat exchange surfaces within a boiler (water-wall, superheater, reheater and economiser tubes) at lower temperatures, and

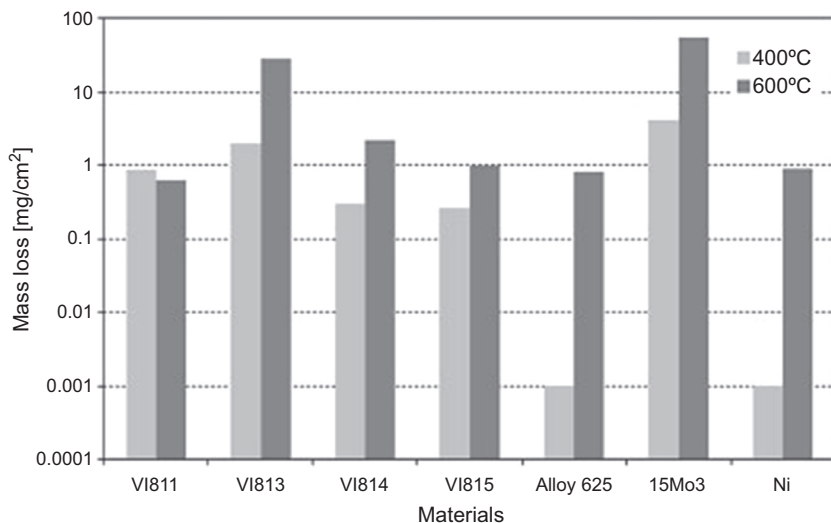


FIGURE 12.10 Alloy weight losses (note log scale) in 300 h exposure to $\text{N}_2\text{-8O}_2\text{-15H}_2\text{O}$ containing 2000 ppm HCl plus 200 ppm SO_2 . The Vxxx alloys are Al + Si modified Fe-9Cr model alloys and 15Mo3 is a low alloy steel [37]. Published with permission, Wiley-VCH.

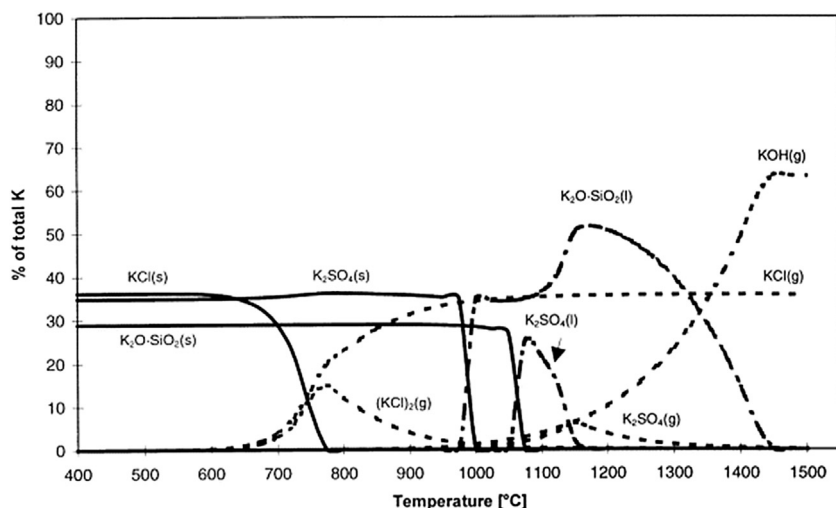
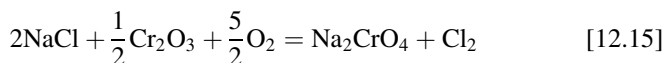
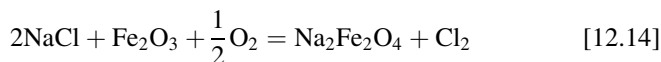


FIGURE 12.11 Thermodynamically stable species of potassium produced in straw combustion. Reprinted from H.P. Nielsen, L.L. Baxter, G. Sclippab, C. Morey, F.J. Frandson, K. Dam-Johansen, *Fuel* 79 (2000) 131 with permission from Elsevier.

condensation of solid KCl results. Interactions between chloride deposits and alloy-oxide scales must therefore be considered.

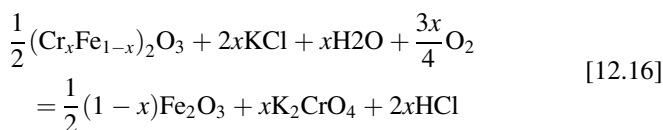
The introduction of NaCl particles onto the oxide scale on steel causes rapid damage in the form of blistering and cracking [38,39]. An immediate increase in oxidation rate was observed for a 2.25Cr-1Mo steel [40] at 450–650°C, and for chromia-forming steels at 700°C [41], when solid NaCl was placed on steels undergoing oxidation in He-O₂. The reaction product was in all cases a poorly adherent, porous scale of Fe₂O₃, with underlying FeCl₂ in the case of the low alloy steel. The source of chlorine was obviously the salt deposit, and the following reactions were proposed



Alkali metal chromate formation has also been reported by Shinata [42] and Shu et al. [43].

Formation of alkali metal chromate has been confirmed by Petterssen et al. [44,45] for the case of 304 stainless steel coated with KCl particles and reacted with N₂-5%O₂ at 600°C. These authors used EDS and Auger electron spectroscopy (AES) to show that K and Cr were located together at the scale surface, and XRD to identify the chromate phase. They also found chlorine at the scale-alloy interface, but at very low levels. The principal mechanism of

scale degradation was thought to be removal of Cr from a mixed (Fe,Cr)₂O₃ scale, leaving a nonprotective iron-rich oxide:



Potassium was found not only at the site of the originally deposited KCl particles, but between them on the scale surface, a phenomenon attributed to the vaporisation of KCl. A plan view of a chromia scale in contact with KCl is shown in Fig. 12.12, where the chromate is seen to develop over much of the scale surface [46]. Loss of KCl from the original deposit is confirmed by the image in Fig. 12.13, where the former site of a salt particle is seen to be marked by a hollow iron-rich oxide shell. The mass transfer processes supporting growth of this oxide have not been clearly identified.

The chromium depletion mechanism does not, of course, apply to low alloy steels which grow iron oxide scales and clearly form FeCl₂ at the scale-gas interface. In all salt deposit accelerated corrosion processes, the mechanisms of scale degradation are available only until the salt is consumed by irreversible reactions such as chromite or ferrite formation, or the chlorine is lost by volatilisation. Steels with sufficiently high chromium levels can sustain a thin, protective chromium-rich oxide scale, even though chromium is depleted

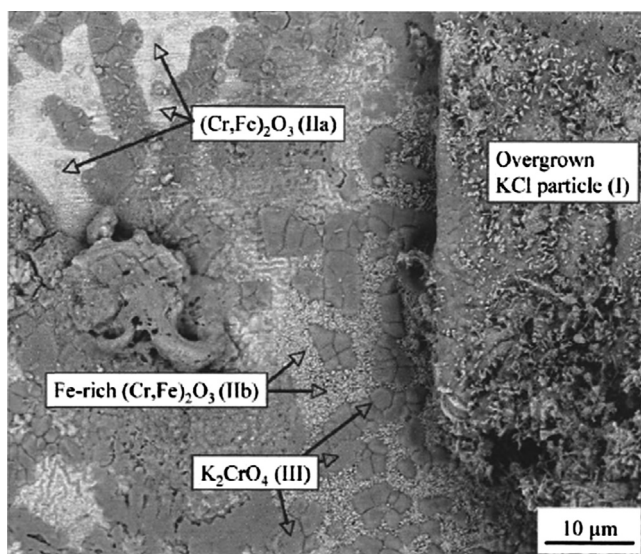


FIGURE 12.12 Plan SEM views of scale surface on Sanicro 28 with 0.1 mg cm⁻² of KCl after one-hour exposure to N₂-5%O₂-40%H₂O at 600°C. Reprinted from C. Proff, T. Jonsson, C. Pettersson, J.-E. Svensson, L.-G. Johansson, M. Halvarsson, in: G.J. Tatlock, H.E. Evans (Eds.), *Microscopy of Oxidation*, Science Reviews (2008) 93 with permission from Science Reviews.

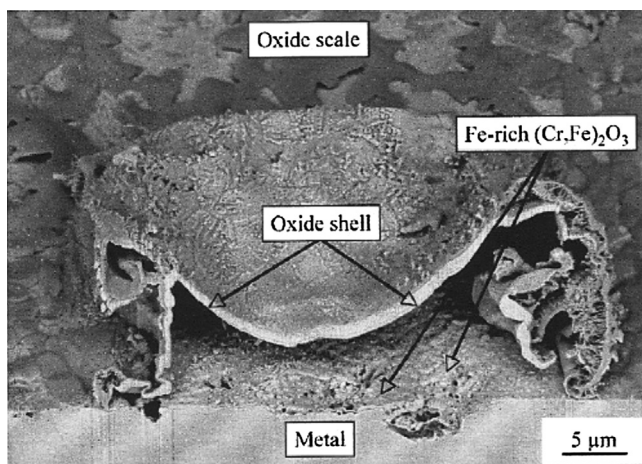


FIGURE 12.13 SEM image of section FIB milled through a former KCl particle after reaction on scale surface of Sanicro 28 as in Fig. 12.12. Reprinted from C. Proff, T. Jonsson, C. Pettersson, J.-E. Svensson, L.-G. Johansson, M. Halvarsson, in: G.J. Tatlock, H.E. Evans (Eds.), *Microscopy of Oxidation*, Science Reviews (2008) 93 with permission from Science Reviews.

by reactions such as Eq. [12.16], provided that the extent of the latter process is limited. The example of Sanicro 28 (Fe-31Ni-27Cr) given a surface coating of 0.1 mg cm^{-2} of KCl particles and exposed to oxidising gases at 600°C is shown in Fig. 12.14 [46]. An initial period of accelerated reaction is followed by protective behaviour because the salt effect vanishes.

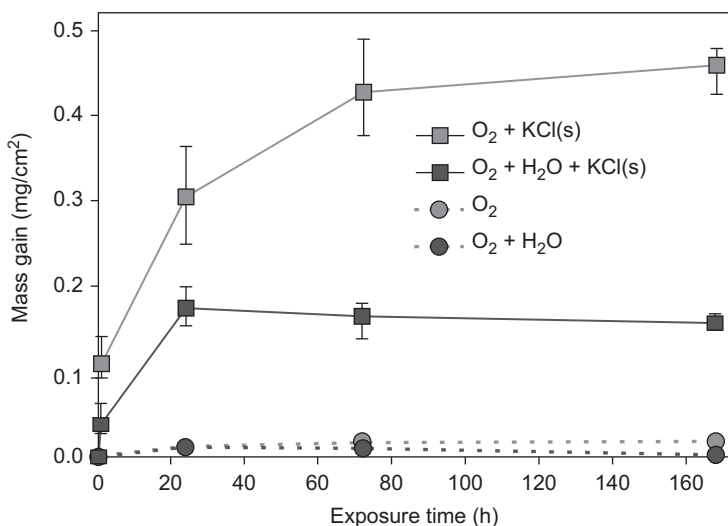
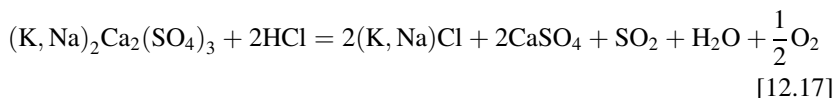


FIGURE 12.14 Effect of 0.1 mg cm^{-2} deposit of KCl on weight gain kinetics of Sanicro 28 at 600°C in N_2 -5% O_2 and N_2 -5% O_2 -40% H_2O . Reprinted from C. Proff, T. Jonsson, C. Pettersson, J.-E. Svensson, L.-G. Johansson, M. Halvarsson, in: G.J. Tatlock, H.E. Evans (Eds.), *Microscopy of Oxidation*, Science Reviews (2008) 93 with permission from Science Reviews.

In continuous combustion processes, the supply of chlorine and alkali-bearing materials is maintained, and the salt removal process observed in the laboratory is not expected to occur. In reality, deposits contain sulphates as well as chlorides (in addition to inert substances such as silica and silicates), and interactions between gas phase ($\text{HCl} + \text{SO}_2$) and the deposits are important to the corrosion reaction [40,41,47,48]. When p_{HCl} is high and p_{SO_2} is low, as in waste or biomass combustion, conversion of deposited sulphates to chlorides is favoured:



The additional chloride can then participate in reactions such as Eqs [12.14]–[12.16], thereby promoting corrosion. Conversely, when p_{SO_2} is relatively high and p_{HCl} low, as in coal combustion, the reverse of Eq. [12.17] is favoured, and conversion of chlorides becomes possible:



Thus harmful chlorides are replaced by less volatile sulphates. Most of the chlorine is produced within the bulk of the deposit rather than at the scale surface and can diffuse to the gas phase and be carried away.

This description of chloride attack resulting from the laboratory studies outlined above has been used to arrive at an understanding of corrosion taking place in biomass-fired boilers and waste to energy plants [4,49,50]. An example of the corrosion morphology developed by a 347 grade stainless steel is shown in Fig. 12.15. The outer scale was iron and chromium-rich, and the underlying porous layer clearly corresponded to selective removal of chromium. Comparison with the laboratory results in Fig. 12.6 shows the similarity in chromium removal by volatilisation.

The use of sulphur to mitigate the effects of KCl on boiler corrosion has been under investigation for a very long time [51,52]. A convenient way of introducing sulphur is through co-firing waste or biomass with coal of suitable sulphur content. This has the added advantage of increasing the energy value of the boiler feed material. In general [51,53], co-firing leads to corrosion at rates slightly above those caused by the high sulphur coal fired alone, but much slower than in the case of waste or biomass fired alone. Plant trials [54] show that the form of corrosion developed during co-firing is very similar to that during firing with the coal alone. The practical difficulties with this strategy relate to the need to achieve a constant, uniform combustion gas composition.

Alternative sources of sulphur added to boiler feed materials with the aim of mitigating chloride corrosion include $(\text{NH}_4)_3\text{SO}_4$ [52], sewage sludge [55], peat [52] and elemental sulphur itself [53,56]. Achieving the correct S-Cl balance is clearly important, as an excess of sulphur exacerbates corrosion by promoting internal sulphidation. Laboratory experiments designed to investigate corrosion of 347 stainless under the conditions of a biomass-fired

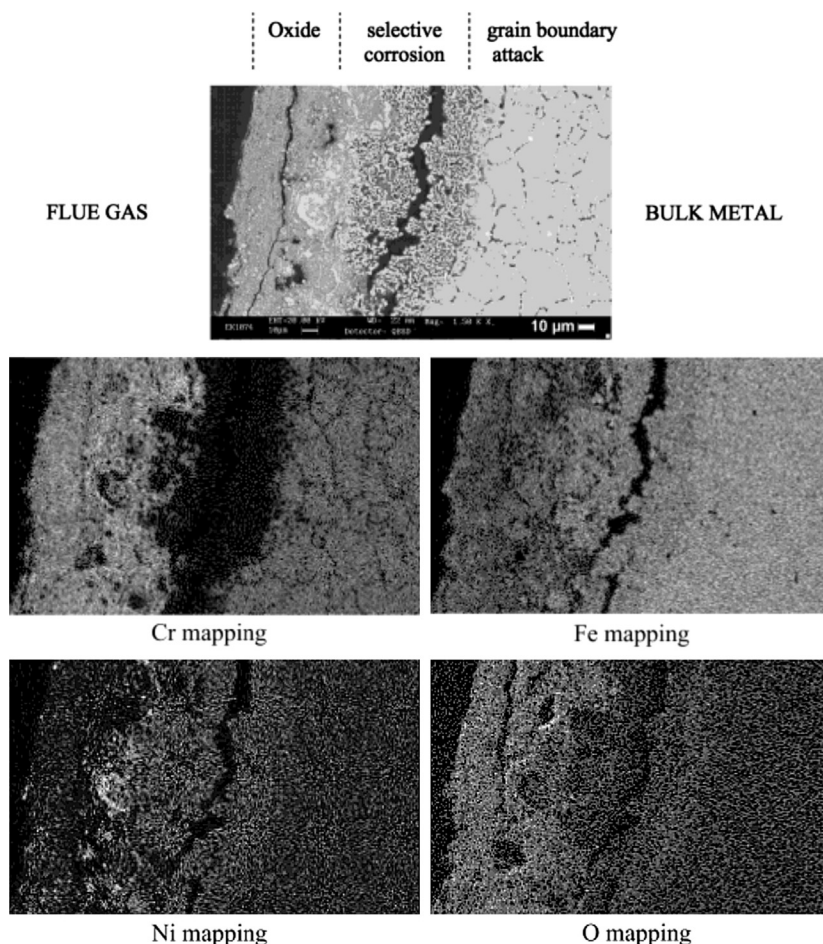


FIGURE 12.15 Type 347H stainless steel exposed in a straw-fired power plant with steam temperature 495°C and a calculated metal temperature 525°C [49]. *Published with permission, Wiley-VCH.*

boiler were carried out by depositing KCl particles on the metal surface and exposing it to flowing gas containing 400 ppm HCl and 60 ppm SO₂ [57]. After 168 h exposure at 560°C, KCl remained on the surface, and corrosion was continuing. Reaction between KCl and the oxide scale was as described by Pettersson et al. [44–46] (Eq. [12.16]) but also involved sulphur penetration of the scale and its reaction with nickel enriched by the removal of chromium and iron.

Because the overall chemistry of the fuel, flue gas, deposit and alloy system is so complex, models have been developed to predict alloy corrosion and its dependence on temperature and fuel mix [58–60]. These models are based on

field and laboratory observations and are therefore limited to the range of conditions examined. If the temperature is in the appropriate range the sulphate deposits will melt, and Type II hot corrosion (Section 8.8) becomes an issue.

An alternative approach to the challenge of achieving high efficiency in the extraction of energy from biomass is to gasify it, producing syngas for later conversion to liquid fuels. The product gas contains alkali chlorides and sulphates, but metal surface temperatures are higher, and the oxygen potentials much more reducing than in combustion systems. Research in this field of corrosion is now commencing [61,62].

Alumina-forming Kanthal alloys are also subject to accelerated attack when KCl particles are deposited on the metal surface before reaction at 600°C [63,64]. Although these alloys form Al-rich oxide films, they are very thin at low temperatures and contain significant levels of chromium and iron incorporated during the initial transient stages of oxidation (Section 5.7.1). When KCl is present at this stage, it reacts to form chromate via Eq. [12.15] or Eq. [12.16], as shown by EDAX and XRD. The alloy then goes into breakaway, forming a nonprotective scale. In an atmosphere of N_2 - O_2 or N_2 - O_2 - H_2O , nitrogen passes through this scale, internally precipitating aluminium nitride, thereby preventing any repassivation. However, if Kanthal APMT (21Cr-5Al-3Mo-0.7Si-Y,Zr,Hf,Ti) is preoxidised in the absence of KCl at 700°C for 24 h, it develops an almost pure alumina layer, which resists attack at 600°C after a KCl deposit has been added [63].

Deposits formed within waste-fired boilers also contain heavy metal chlorides, notably $PbCl_2$ and $ZnCl_2$ (Table 12.1). As seen in Table 12.3, these salts have very low melting points, and the effect of molten salts on corrosion must be considered.

12.4 CORROSION BY MELTS

As seen above, chlorides are commonly present in municipal waste and various forms of biomass. Combustion of these materials leads to flue gases containing HCl and alkali chloride vapours. The consequent corrosion of boiler materials is severe at high temperatures, necessitating operation of these power units at lower temperatures. As a result, generation efficiencies are low, and the need for improvement is driving research on chloride corrosion-resistant materials.

Halide melts are also of interest as heat transfer and thermal storage media, where a combination of low melting point and high thermal stability is required [65,66]. Thus, for example, the ternary eutectic (LiF-11.5 mol% NaF-42 mol% KF) has a melting point of 454°C and a boiling point of 1570°C. It also has a high heat capacity, thermal conductivity and specific heat, making it a candidate for use as a reactor primary coolant and as a solar thermal heat transfer and energy storage medium [67].

12.4.1 Molten Halides

As seen in Table 12.3, metal chlorides have rather low melting points. Those of metal fluorides are higher (Table 12.5), but eutectics formed by halide mixtures melt at much lower temperatures, as seen in Table 12.6 [68]. Alkali metal halides are thermodynamically stable with respect to common metal halides, and a comparison is shown for fluorides in Fig. 12.16 [67].

Liquid halides are ionic melts, and their corrosion of metals is therefore an electrochemical process, involving anodic dissolution of metal:



As is clear from Fig. 12.16, the cathodic process cannot be reduction of an alkali metal cation. In a pure fluoride melt, no other oxidant is available and corrosion therefore cannot occur. An experimental demonstration for the case of an LiCl-based melt was provided by Indacochea et al. [69,70]. Several stainless steels and a low alloy steel were exposed to the melt at 725°C under argon for 30 days, but did not corrode. However, when Ar-10% O₂ was bubbled through the melt, corrosion of these materials was extensive, leading to formation of nonprotective oxides. Similarly, Mansfield et al. [71] showed that chromia-forming superalloys were corroded by molten sodium chloride at 820°C to form nonprotective oxides at rates which were very sensitive to oxygen and water vapour pressures. Clearly, it is the oxygen impurity which is responsible for molten halide corrosion.

The thermodynamics of corrosion in fused halide salts were analysed by Edeleanu and Littlewood [72] long ago in terms of acid-base behaviour, and that treatment continues in use. Just as in the case of molten sulphate hot corrosion (Section 8.8.2), the melt basicity, pO^{2-} , is defined as

$$pO^{2-} = -\log a_{O^{2-}} \tag{12.20}$$

TABLE 12.5 Metal Fluoride Melting Points	
Salt	MP (°C)
LiF	845
KF	858
NaF	993
PbF ₂	855
ZnF ₂	872
CrF ₂	1100
AlF ₃	1291

TABLE 12.6 Halide Eutectic Melting Points		
System	Composition (mol %)	MP (°C)
AlCl ₃ -KCl-NaCl	63.5–16.5–20	88
AlCl ₃ -NaCl	34–66	93
AlCl ₃ -FeCl ₃ -NaCl	48–3–49	145
CrCl ₂ -KCl-NaCl	17.2–37.8–45	442
FeCl ₃ -KCl	47–53	202
FeCl ₃ -PbCl ₂	37–63	177
FeCl ₃ -KCl-LiCl	51–17–32	110
KCl-K ₂ CrO ₄	32–68	650
KCl-ZnCl ₂	49–51	230
KCl-PbCl ₂ -ZnCl ₂	42–6–52	210
PbCl ₂ -ZnCl ₂	93–7	242
CaF ₂ -LiF-NaF	11.1–51.1–37.8	607
FeF ₃ -NaF	65–35	892
KF-LiF-NaF	42–46.5–11.5	454

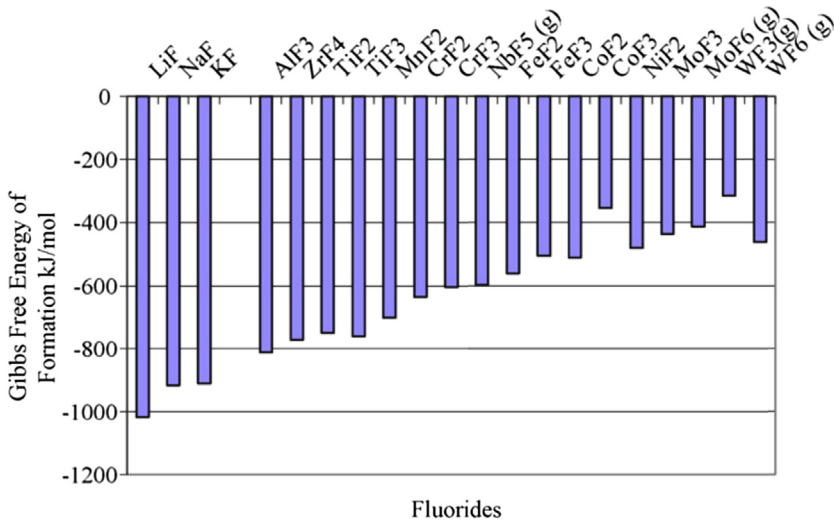
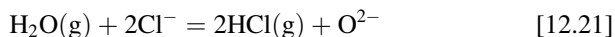


FIGURE 12.16 Relative stability of fluorides at 850°C. Reprinted from L.C. Olsen, J.W. Ambrosek, K. Sridharan, M.H. Anderson, T.R. Allen, *J. Fluorine Chem.* 130 (2009) 67 with permission from Elsevier.

where in this case the oxygen anions derive from interaction with the gas phase, eg,



for which at equilibrium

$$0 = 2\mu_{\text{HCl}} + \mu_{\text{O}^{2-}} - \mu_{\text{H}_2\text{O}} - 2\mu_{\text{Cl}^-} \quad [12.22]$$

Expanding the chemical potential terms and setting the chloride activity $a_{\text{Cl}^-} = 1$ for an almost pure chloride melt, one obtains

$$2.303p\text{O}^{2-} = \Delta G_{21}^\circ / RT + \ln \frac{p_{\text{HCl}}^2}{p_{\text{H}_2\text{O}}} \quad [12.23]$$

where ΔG_{21}° is the standard free energy change for reaction [12.21]. Thus the basicity is defined for a particular temperature by the partial pressures of HCl and H₂O. This in turn determines the driving force for the destruction of otherwise protective oxides by basic dissolution (Eq. [8.19]) or acidic dissolution (Eq. [8.20]).

The equilibrium constant for Eq. [12.21] was evaluated electrochemically for equimolar NaCl-KCl melts at temperatures of 700–1000°C by Combes et al. [73]. Their measurements correspond to

$$\Delta G_{21}^\circ = 1,058,800 - 770 T \text{ (J mol}^{-1}\text{)} \quad [12.24]$$

and basicity can be calculated. This information was used by Ishitsuka et al. [74] in measuring oxide solubilities as a function of basicity in molten NaCl-KCl. Their results in Fig. 12.17 show the very high solubility of Cr₂O₃, and account for the preferential removal of chromium from iron and nickel-base alloys in chloride melts. The accompanying data for dissolution in NaCl-KCl-Na₂SO₄-K₂SO₄ eutectic illustrates the preferential attack on chromium which also occurs under basic conditions in the mixed salt. Basicity values in the latter case are not precise, as the partial pressure of SO₃ was not controlled.

The solubility of Cr₂O₃ in both acidic and basic chloride melts can also be represented on a Pourbaix (potential - $p\text{O}^{2-}$) diagram, as shown in Fig. 12.18 [74,75]. In highly basic conditions, chromia is oxidised to form soluble chromate or dichromate. Under acidic conditions, it dissolves dissociatively into cations and anions. Protection of chromia can be achieved if the salt basicity can be adjusted to values corresponding to solid chromia stability. In the case of waste incinerators, this means increasing the $p\text{O}^{2-}$ value. This can be done if the alloy contains Mo, V or W, all of which form acidic oxides [74]. The beneficial effect of molybdenum in resisting chloride accelerated attack has been reported in several instances [76–78].

12.4.1.1 Fluxing in Chloride Melts

If the molten salt film on a metal surface was homogeneous, then oxide dissolution would cease once the solubility limit was reached. The reason that

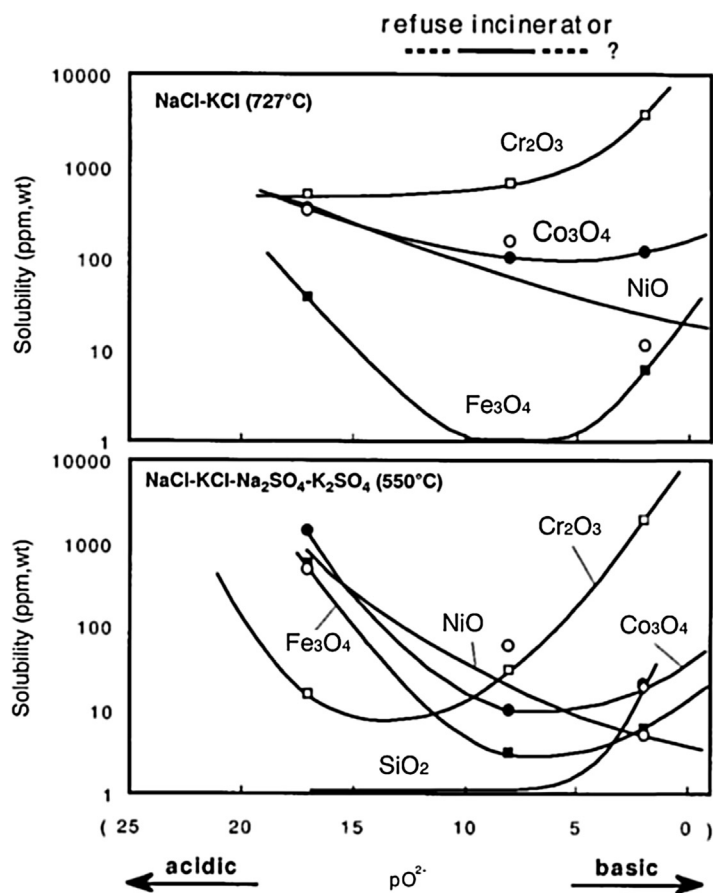


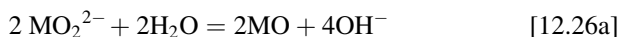
FIGURE 12.17 Measured oxide solubilities in molten salts at controlled basicity values [74].
Published with permission, Wiley-VCH.

corrosion continues in practice is the existence of chemical potential gradients across the thickness of the film, as shown schematically in Fig. 12.19. Oxide ions are generated at the salt-gas interface through reaction with H_2O , and consumed at the scale-salt interface in the basic dissolution process



The resulting gradient in basicity drives inward diffusion of oxide anions, continuing the dissolution process.

Metal-containing species diffuse outward from the oxide-salt interface, toward the salt film surface. Here high oxidant activities resulting from interaction with the surrounding gas cause precipitation reactions such as



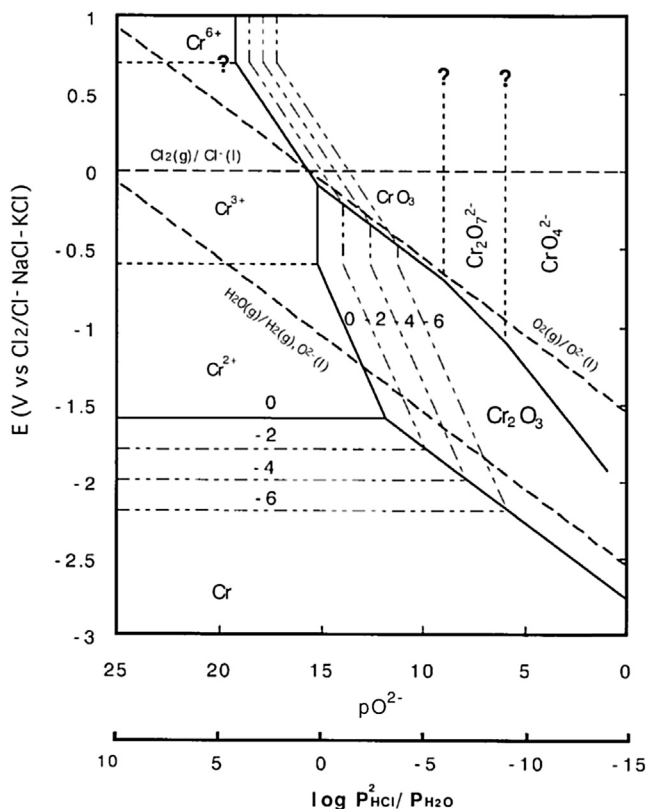
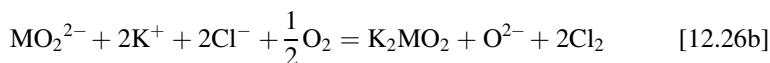


FIGURE 12.18 Potential (E) – basicity diagram for Cr in molten NaCl-KCl eutectic at 727°C [74,75]. Published with permission, Wiley-VCH.

or



The precipitated oxide is porous and nonprotective, allowing the dissolution-reprecipitation process to continue. Fluxing in chloride melts is seen to be closely similar to the process occurring in molten sulphate accelerated hot corrosion (Section 8.8.3).

A number of investigations into corrosion in low melting chloride salts have been undertaken due to its importance in limiting the performance of waste incinerators. Because both potassium and zinc are commonly present, very low melting point chlorides can form (Fig. 12.20 [79]). The reaction products are found to be porous or particulate metal oxides embedded in the salt and reflect the operation of a fluxing process. A typical example in Fig. 12.21 [80] shows extensive corrosion of nickel in an equimolar KCl-ZnCl₂ mixture under Ar-8% O₂ at 320°C. Similar reaction morphologies were found for corroded iron and

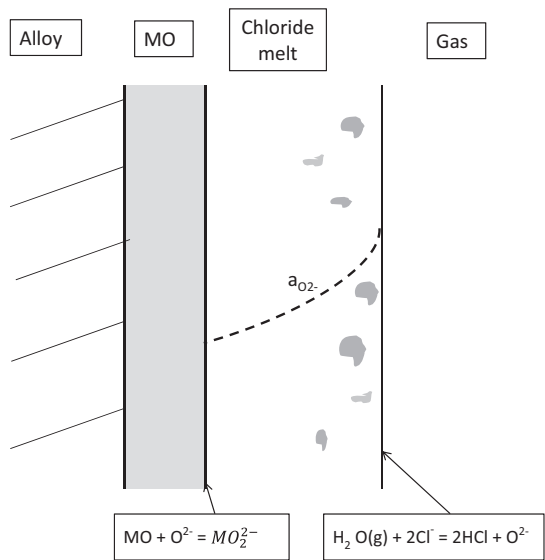


FIGURE 12.19 Molten chloride corrosion by dissolution and reprecipitation of oxide.

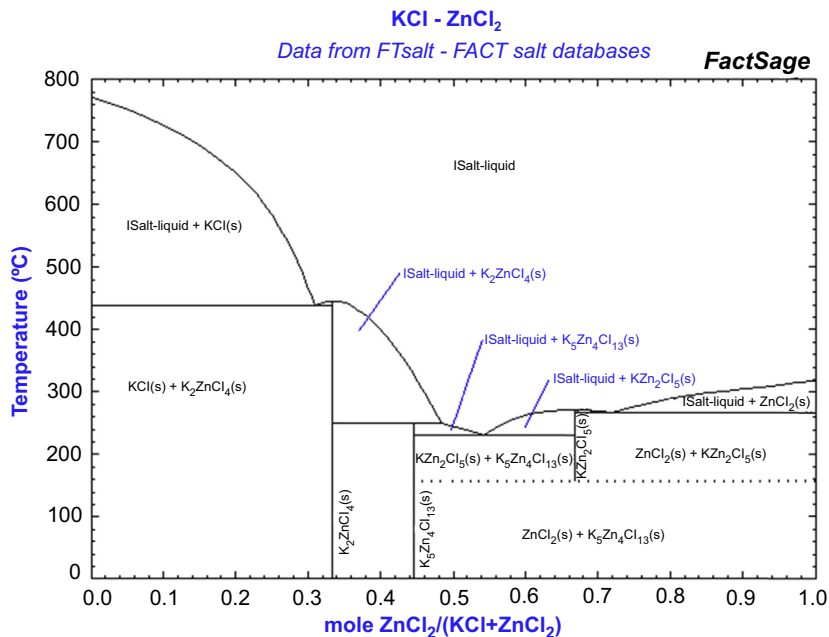


FIGURE 12.20 Phase diagram for KCl-ZnCl₂ [79].

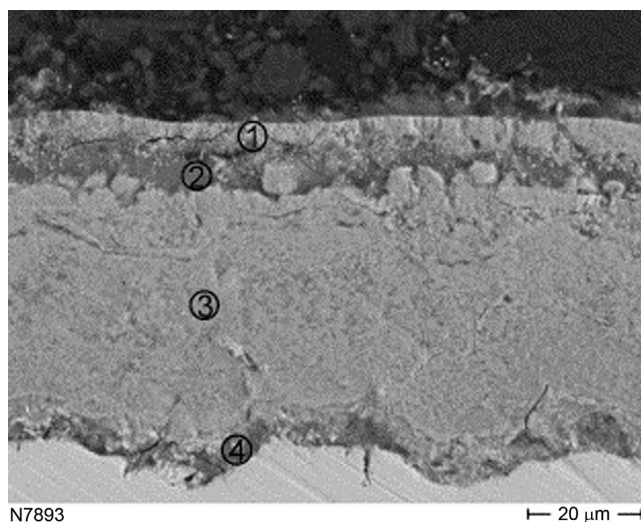


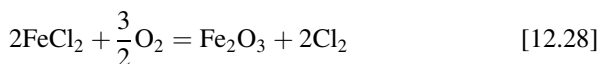
FIGURE 12.21 Cross-section of reaction product on pure nickel after exposure at 320°C to KCl-ZnCl₂, showing an outer NiO-rich layer (1), chloride melt layers (2 + 4) and precipitated nickel oxide within the molten chloride (3). Reprinted from A. Ruh, M. Spiegel, *Corros. Sci.* 48 (2006) 679 with permission from Elsevier.

chromium at this temperature [80], and for the chromia formers 310 stainless and HP grade (25Cr-35Ni) heat-resisting steel [81] at 450°C.

In the molten salt corrosion literature, reactions are commonly described in molecular rather than ionic terms [46,47,80,82,83]. Thus basic fluxing of iron in chloride melts is written as



for reaction at the metal-salt interface, where the oxygen activity is low, and

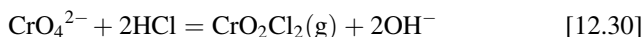


beneath the salt-gas interface, where oxygen is supplied from the environment. Inward transport of Cl₂ and outward transport of metal chloride support the continued ‘cycling’ of chlorine, and the description is seen to be closely similar to that shown in Fig. 12.3.

Dissolution of otherwise protective oxide into the molten salt is conventionally written in the form of reaction [12.16]. In the case of chromium under a chloride melt, this is verified by the finding [80] of water soluble chromate species in the surface deposit after reaction and is in agreement with the predictions of Fig. 12.18. The chromia dissolution reaction could also be expressed in equivalent ionic form:



at the scale-melt interface. At the melt surface, where the basicity is higher, the chromate would remain in solution, and fluxing would cease. However, if the temperature is high enough, oxychloride formation is possible

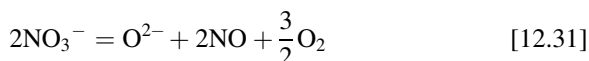


and catastrophic corrosion occurs.

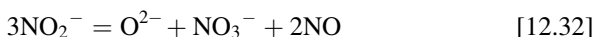
12.4.2 Oxygenated Melts

Corrosion in sulphate melts, or ‘hot corrosion’, is considered in Section 8.8.1. Fused salts containing other oxyanions are also of technical interest and can cause corrosion in a similar way. Mixed nitrate and nitrate-nitrite melts have been suggested [66] for use as heat transfer and energy storage media in concentrated solar thermal power generation. Rather low melting point mixtures are available: NaNO_3 -44 KNO_3 -49 NaNO_2 (mol%) melts at 151°C [84]. Mixed carbonate melts are also candidates for this application, with better high-temperature stability than the nitrates [85]. Technical interest in carbonate melts commenced earlier with the development of the molten carbonate fuel cell.

The thermodynamics of these oxyanion melts can be described, like those of sulphates, in terms of equilibrium with the oxide anion and appropriate gas species. For a nitrate melt



for a nitrite



and for a carbonate



In addition, the equilibrium



represents Eqs [12.31] and [12.32], and any two of Eqs [12.31], [12.32] and [12.34] describe the nitrate-nitrite system.

12.4.3 Corrosion in Nitrate/Nitrite Melts

The thermodynamics of equimolar NaNO_3 - NaNO_2 melts in equilibrium with water vapour have been established [86–88], and the water vapour equilibrium determined to be



as shown in Fig. 12.22. Data for reactions [12.32], [12.34] and [12.35] are summarised in Table 12.7.

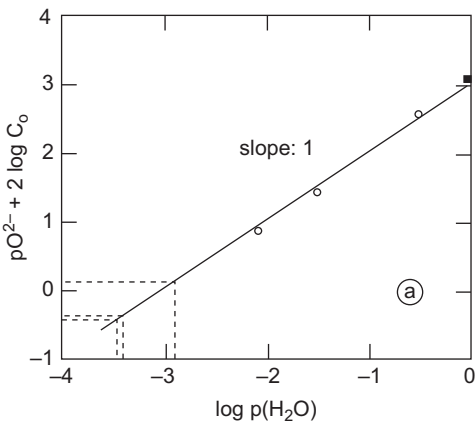


FIGURE 12.22 Variation of basicity, pO^{2-} , with water vapour partial pressure measured in equimolar $NaNO_3$ - $NaNO_2$ at $420^\circ C$. Here C_0 is the original concentration of hydroxide [88], with permission from the *Electrochemical Society*.

Picard et al. [87,88] used this information, together with electrochemical measurements for iron immersed in melts of different basicity values, to construct a Pourbaix diagram. Solid reaction products were, on this basis, predicted to be Fe_2O_3 , $NaFeO_2$ and $Na_4Fe_2O_5$, and their stability regimes and solubilities are shown in Fig. 12.23. Thus iron oxide is predicted for acidic melts, FeO_2^- for mildly basic conditions and $Fe_2O_5^{4-}$ for strongly basic conditions. The formation of iron oxide scales in nitrate and nitrate/nitrite melts has been reported many times (for example, [89–91]). Ferrate has been identified by XRD on carbon steel [92] and 2.25Cr-1Mo steel [93] corroded in $NaNO_3/NaNO_2$, and on stainless steels in mixed nitrates [93,94]. Salts of the more basic $Fe_2O_5^{4-}$ have been reported [94] to form on carbon steel in mixed nitrate melts.

Type 304 stainless steel performs much better than carbon or alloy steels when exposed at moderate temperatures to nitrate melts at $550^\circ C$ [93]. However, 430 stainless is nonprotective under the same conditions. Both alloys develop $FeCr_2O_4$ as a principal reaction product, as a coherent scale layer on 304, but as

TABLE 12.7 Thermodynamics of Equimolar $NaNO_3$ - $NaNO_2$ Melts [86,88]		
Reaction	$\Delta G^\circ = A + BT \text{ (J mol}^{-1}\text{)}$	
	<i>A</i>	<i>B</i>
$NO_3^- = NO_2^- + \frac{1}{2} O_2$	104,930	−104.7
$3NO_2^- = 2NO + NO_3^- + O^{2-}$	305,820	−302.7
$2OH^- = H_2O(g) + O^{2-}$	104,930	−91.9

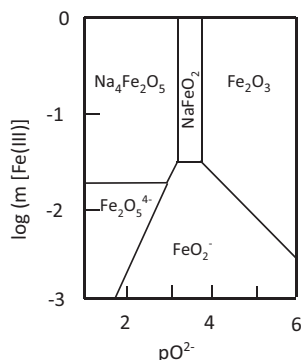


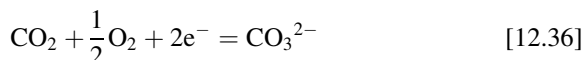
FIGURE 12.23 Stability diagram for iron species and solubilities in nitrate-nitrite melts as a function of basicity at $T = 500^\circ\text{C}$. *G.S. Picard, H.M. Lefebvre, B.L. Tremillon, J. Electrochem. Soc. 134 (1987) 52, with permission from the Electrochemical Society.*

multiple striations within a thick scale in the case of the ferritic alloy. The mechanisms of scale formation under these conditions are not yet available.

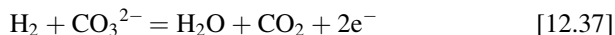
Finally, it is noted that whereas nitrate melts are not highly corrosive at moderate temperatures, the presence of chloride impurities makes them much more aggressive [90,91,93].

12.4.4 Corrosion in Carbonate Melts

Molten carbonate fuel cell technology is well-established [95], and a substantial body of research on corrosion in the melts has accumulated. In these cells the cathode process is



and the anode process



The structure of a molten carbonate fuel cell is similar to that of a solid oxide fuel cell (Fig. 11.8), but the chemistry is of course different. The electrolyte is a carbonate melt, commonly based on the eutectic mixture 63% Li_2CO_3 -38% K_2CO_3 (mol basis), supported by a porous LiAlO_2 ceramic, the anode gas is $\text{H}_2 + \text{CO}$ and the cathode gas is air + CO_2 . As seen in the figure, the anode, cathode and interconnect/separator plates are in contact with the melt. In addition, metallic seals also contact the molten carbonate.

12.4.4.1 Nickel Oxide Corrosion by Carbonate Melts

Lithium-doped nickel oxide is used for the cathode in molten carbonate fuel cells, and its solubility in carbonate melts has been studied intensively. Early work [96–98] established that NiO solubility in carbonate melts was controlled by their basicity and temperature (Eq. [12.33]) and was independent

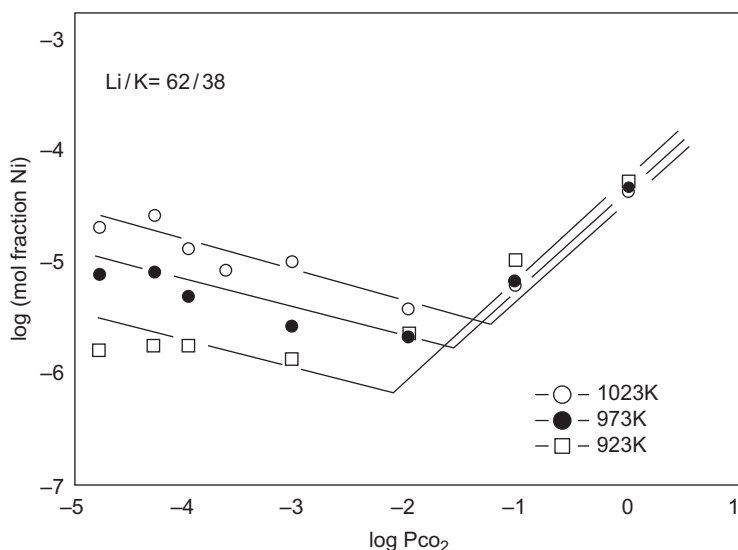


FIGURE 12.24 Solubility of NiO in $\text{Li}_2\text{CO}_3\text{-K}_2\text{CO}_3$ eutectic melt as a function of basicity. *K. Ota, S. Asano, H. Yoshitaka, N. Kamiya, J. Electrochem. Soc. 139 (1992) 667, with permission from the Electrochemical Society.*

of oxygen partial pressure. Solubility data [99] for $\text{Li}_2\text{CO}_3\text{-K}_2\text{CO}_3$ eutectic melts in Fig. 12.24 show that in acid melts,

$$\frac{d\log N_{\text{NiO}}}{d\log p_{\text{CO}_2}} = 1 \quad [12.38]$$

in agreement with the equilibria Eq. [12.33] and that for acid dissolution at high CO_2 partial pressures:



In basic melts, however,

$$\frac{d\log N_{\text{NiO}}}{d\log p_{\text{CO}_2}} = -0.3 \quad [12.40]$$

also independent of oxygen partial pressure. The conventional NiO basic dissolution reaction [8.19] cannot apply, whereas the dependency predicted for anaerobic basic dissolution



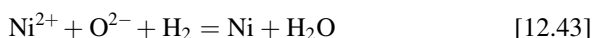
is

$$\frac{d\log N_{\text{NiO}}}{d\log p_{\text{CO}_2}} = -1 \quad [12.42]$$

Because molten carbonate fuel cells operate under acid conditions, research has been focused on this regime.

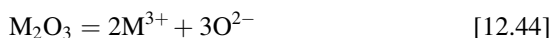
The temperature effects seen in Fig. 12.24 reflect the temperature sensitivity of the carbonate decomposition reaction [12.33]. Under acid conditions, solubility decreases with increasing temperature because increased O^{2-} concentrations resulting from carbonate decomposition drive the acid dissolution reaction [12.39] to the left. Under basic conditions, the effect is reversed, with NiO solubility increasing with temperature. Higher O^{2-} concentrations promoting basic dissolution reactions, such as Eq. [12.41], account for this observation.

Nickel oxide solubilities in carbonate melts are quite low, and saturation of the cell electrolyte might, on that basis, be expected to limit cathode corrosion losses. However, in the fuel cell, hydrogen from the anode reduces the nickel solute to the metallic state



and metal precipitates as solid within the melt. This dissolution-reprecipitation process is similar to fluxing, as it drives continuing corrosion. In addition, the solid nickel can short out the cell, an obviously undesirable result.

Dissolution of selected rare earth oxides in carbonate melts has been investigated under acidic conditions [100,101], with the intention of reducing NiO solubility. Solubility results for several rare earths in $\text{Li}_2\text{CO}_3\text{-Na}_2\text{CO}_3$ eutectic mixture at 650°C are seen in Fig. 12.25 to differ widely. The different responses to changing values of p_{CO_2} indicate different stoichiometries of the dissolution reactions. The simple acidic dissolution process



combined with Eq. [12.33] to yield

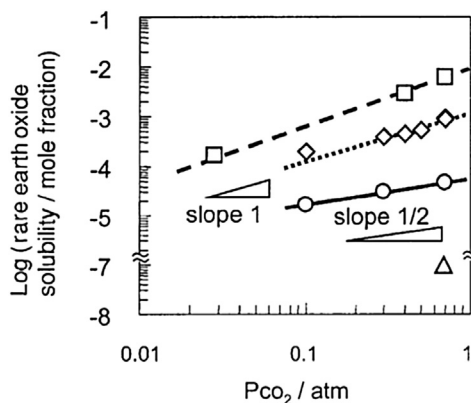


FIGURE 12.25 Solubility of selected rare earth oxides in $\text{Li}_2\text{CO}_3\text{-Na}_2\text{CO}_3$ eutectic melt at 650°C and $p_{\text{CO}_2}/p_{\text{O}_2} = 7/3$: La (□), Gd (◇), Y (○) and Ce (Δ). K. Matsuzawa, T. Mizusaki, S. Mitsushima, N. Kamiya, K. Ota, *J. Power Sources* 140 (2005) 258; K. Matsuzawa, G. Tatezawa, Y. Matsuda, S. Mitsushima, N. Kamiya, K. Ota, *J. Electrochem. Soc.* 152 (2005) A1116, with permission, the Electrochemical Society.



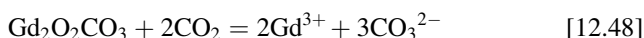
predicts

$$N_{\text{M}} = Kp_{\text{CO}_2}^{3/2} \quad [12.46]$$

at variance with experimental result. Instead, the reactions



and



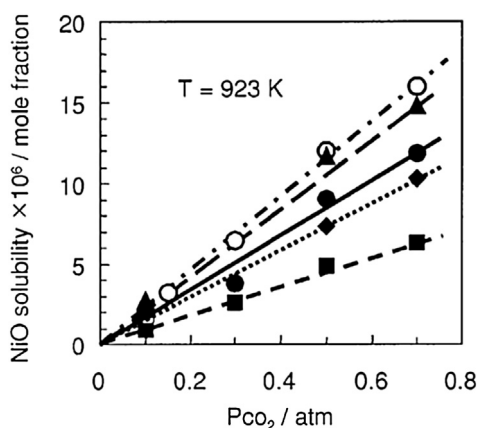
were suggested [101], the latter being supported by XRD identification of the oxycarbonate in the solidified melt.

Whatever the precise mechanism of acidic dissolution, it is clear that the process makes the melt more basic, and according to Fig. 12.24, the solubility of NiO in the modified melt is thereby reduced. The effect is illustrated in Fig. 12.26, where the reduction in NiO solubility is greatest for the most soluble rare earth oxide. The low solubility of CeO₂ is exploited in the use of ceria coatings to protect NiO cathode in carbonate fuel cells [102].

12.4.4.2 Iron and Chromium in Carbonate Melts

Because oxide-melt interactions in carbonates are acid-base reactions, their products are expected to be the same as those produced in nitrates. However, the oxygen potential can vary in carbonate melts, rather than being buffered by the nitrate-nitrate equilibrium Eq. [12.34]. An examination [103] of the thermodynamics of the Fe-Li-K-C-O system at 650°C reveals a consequently greater diversity of reaction products, as seen in Fig. 12.27.

FIGURE 12.26 Effect of dissolved rare earth oxides on NiO solubility in Li₂CO₃-Na₂CO₃ eutectic melt at 650°C and $p_{\text{CO}_2}/p_{\text{O}_2} = 7/3$: NiO alone (○), Ce saturated (▲), Y saturated (●), Gd saturated (◆) and La saturated (■). K. Ota, S. Asano, H. Yoshitaka, N. Kamiya, *J. Electrochem. Soc.* 139 (1992) 667; K. Matsuzawa, T. Mizusaki, S. Mitsushima, N. Kamiya, K. Ota, *J. Power Sources* 140 (2005) 258; K. Matsuzawa, G. Tatezawa, Y. Matsuda, S. Mitsushima, N. Kamiya, K. Ota, *J. Electrochem. Soc.* 152 (2005) A1116, with permission, the Electrochemical Society.



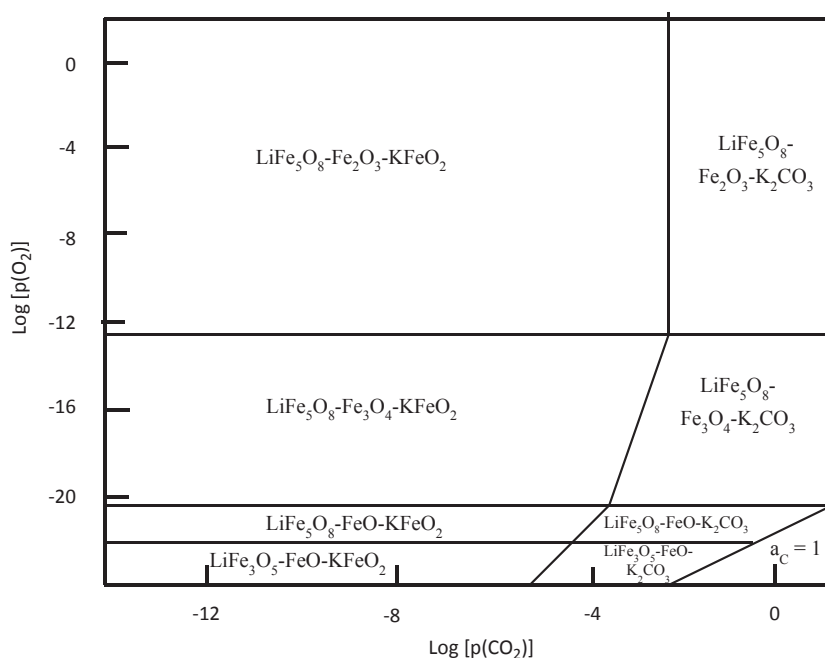
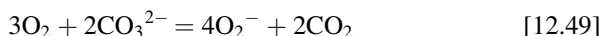


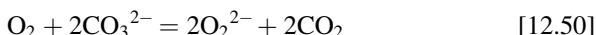
FIGURE 12.27 Thermochemical diagram for Fe-Li-K-C-O at 650°C, with Li:K = 6:4 and salt:Fe = 1:100. H.S. Hsu, J.H. DeVan, *J. Electrochem. Soc.* 133 (1986) 2077, with permission, the Electrochemical Society.

Corrosion of pure iron under a deposit of $\text{Li}_2\text{CO}_3\text{-K}_2\text{CO}_3$ eutectic melt in Ar-20% O_2 -0.01% CO_2 at 650°C produced a multilayer scale consisting of compact FeO and Fe_3O_4 and an outer porous layer of $\text{Fe}_2\text{O}_3 + \text{LiFe}_5\text{O}_8$ [103]. Small amounts of potassium were detected at the scale-melt interface, so the corrosion products were consistent with the prediction in Fig. 12.27 of $\text{Fe}_2\text{O}_3 + \text{LiFe}_5\text{O}_8 + \text{KFeO}_2$. Low alloy steels and dilute iron-base alloys exposed to this melt under N_2 -15% O_2 -15% CO_2 at 650°C formed scales consisting of an outermost LiFeO_2 layer, an intermediate LiFe_5O_8 layer and an innermost Fe_3O_4 layer [48,104], a result also predicted thermodynamically for high salt:iron ratios [103]. In these reactions, iron oxide layer growth is sustained by a reaction with oxygen dissolved in the melt.

Oxygen solubility in Na_2CO_3 is very low [105] and deviates strongly from Henry's law, implying a chemical interaction. Nishina et al. [106] studied reduction of a carbonate melt at an inert metal electrode, concluding that the species being reduced were superoxide ions, O_2^- , and peroxide, O_2^{2-} . Oxygen is dissolved into the melt via



or



Superoxide ions are reduced at the corroding metal surface



and peroxide via Eq. [12.52]. Here the accompanying metal oxidation process



balances the charge.

Thermochemical diagrams have been established [107] for the Cr-Li-K-C-O system at 650°C and a Li:K ratio molar ratio of 6:4. At high oxygen and CO₂ partial pressures (as in the cathode gas of a molten carbonate fuel cell, or in a combustion gas), the predicted chromium corrosion products are K₂CrO₄(s), (Li,K)₂CrO₄(l) and Cr₂O₃, depending on the concentration of chromium in the salt. The liquid mixed alkali chromate is highly soluble in the carbonate melt but forms only when $N_{\text{Li}}/N_{\text{K}} \geq 2$. However, pure chromium covered with a layer of 60/40 lithium-potassium carbonate melt under cathode gas conditions corroded rapidly. The reason was that the initial reaction to form K₂CrO₄ raised the Li/K ratio in the melt, leading to liquid (Li,K)₂CrO₄ formation.

At low oxygen and CO₂ partial pressures, corresponding to anode (fuel) gas, the stable chromium corrosion products are Cr₂O₃ and LiCrO₂(s). The duplex chromia-LiCrO₂ scale developed under these conditions is protective.

12.4.4.3 Chromia-Forming Alloys in Carbonate Melts

Early work on stainless steels under molten carbonate fuel cell conditions [108] established that grades such as 304 and 316 were corroded rapidly, but higher chromium content grades such as 310 or 446 were much more protective, developing a multilayer scale with an inner, compact Cr₂O₃ layer. Simultaneous internal carburisation is observed [95,108]. This results from the high carbon activity expected at low oxygen potentials beneath a chromia scale grown in a carbon-rich environment. The reaction can be formulated as



but requires transport of carbon through the oxide scale. Ways in which this can happen are discussed in Section 10.5.

More detailed analysis of the reaction products of molten carbonate corrosion [104,109–111] show them to be complex, varying with alloy

chromium content. High chromium levels lead eventually to a multilayered scale, consisting of a fissured outermost layer of LiFeO_2 , a layer of LiCrO_2 over spinel with an innermost layer of $(\text{Fe,Cr})_2\text{O}_3$. Lower chromium levels are associated with inner scale spinel layers, and an absence of chromia. Formation of soluble chromate species continues, apparently supported by outward diffusion of the metal.

It has been noted [110] that chloride impurities in the melt accelerate corrosion, producing more porous scales. This is of practical importance in the operation of black liquor recovery boilers to generate steam. Organics extracted from wood chips in the pulping process are combusted, producing ash containing alkali metal chlorides and carbonates. Its deposition on superheater tubes can cause rapid corrosion if a melt forms. Because deposit chemistry varies greatly with plant operation, the practical solution is to limit steam temperatures so that deposits are always below their solidus temperatures [112].

12.5 MANAGING COMPLEX CORROSION

As seen in this chapter, the possibility of either volatile metal compound formation or dissolution into melts complicates the chemistry and mass transfer processes of the corrosion process greatly. Given the multicomponent nature of the media involved — fuels, gases, salt and oxide deposits, as well as corrosion products (solid, liquid and gaseous) — the use of computational thermodynamic analysis is unavoidable. Commercial software is adequate, but databases for melts are limited. Fortunately, these are being updated.

The usual strategies for corrosion control have all been explored in the cases considered in this chapter: modifications to environmental chemistry, selection of more highly alloyed materials and reduction in operating temperature. A major difficulty arises through the inadequacy of chromia-forming alloys in many situations. This is an unavoidable consequence of the metal's chemistry: the volatility of CrO_2Cl_2 and the high solubility of chromia in chloride and carbonate melts. The latter represents a major difference from the relative success of chromium-rich alloys in resisting molten sulphate hot corrosion, where the basicities of the sulphate melts are high enough to reduce Cr_2O_3 solubility.

In contrast, alumina-forming alloys exhibit far better resistance to chlorine attack and to molten chlorides and carbonates. The former is due to the resistance of an alumina scale to penetration by chlorine, and the fact that AlOCl(g) is produced at only extremely low partial pressures. Superior resistance of alumina to molten carbonate attack reflects low solubility of Al_2O_3 in the melt and is evidenced by the successful use of LiAlO_2 ceramic supports for molten carbonate fuel cell electrolyte. Although no measurements of Al_2O_3 solubility in chloride melts have been reported, alumina ceramics have been used as containment materials in chloride melt solubility experiments [74]. The difficulty in using alumina-forming alloys at the relatively

modest temperatures encountered in boilers, solar thermal systems and fuel cells is their frequent failure to form scales made up exclusively of Al_2O_3 . A solution to this problem is provided by the use of Al-rich coatings.

Aluminised stainless steel performs well for wet seals in molten carbonate fuel cells. Unfortunately, it cannot be used as a current collector, because the electrical resistivity of alumina is too high. Sprayed alumina-forming coatings have been tested under waste-fired boiler conditions [113] and simulated biomass-fuelled conditions [114] but were found to fail as a result of penetration along coating splat boundaries. Dense aluminised coatings have been shown to be much more successful, forming protective LiAlO_2 over dense alumina [115,116] in carbonate melts.

Under high chlorine pressures and strongly reducing conditions, Al-rich coatings are unsuccessful at high temperatures, because the highly volatile AlCl_3 is preferentially formed, leaving a porous residue behind. Small additions of molybdenum to NiAl have been found [117] to reduce the corrosion rate in air + 10% Cl_2 at 1000°C. The effect is thought to be due to a slowing of the surface processes involved with evaporation, but details have not been established.

Although metal halide volatility presents a very difficult corrosion problem, it is of benefit in the chemical vapour deposition process, ‘pack cementation’. Within a closed pack, aluminium metal is volatilised at high temperatures by contacting a source metal or alloy powder with an activator such as NH_4Cl . The resulting vapour species permeates through the pack, contacting the surface of a substrate, such as a superalloy turbine blade. At this surface, the vapour species deposits metal which diffuses into the substrate, producing an aluminide coating.

Halide volatilisation is also made use of in achieving protective alumina formation on TiAl. The usual problem with TiAl at high temperatures is that the free energies of formation for TiO_2 and Al_2O_3 from the intermetallic are almost equal. At temperatures above about 750°C, both oxides form, resulting in a nonprotective scale. However, introduction of small amounts of fluorine or chlorine to the system, for example by prior ion implantation, promotes protective alumina scaling [118]. The mechanism is essentially one of ‘active oxidation’, just as observed during oxygen-chlorine attack (Section 12.2.2). It arises from the fact that AlF develops a much higher partial pressure than any titanium fluoride, and the metal is thereby enriched in the growing scale [119,120]. So great is the extent of enrichment, a continuous, protective alumina layer develops.

REFERENCES

- [1] P. Steinmetz, C. Rapin, Mater. Sci. Forum 251–254 (1997) 505.
- [2] A. Show, K. Toyama, K. Nagashima, M. Yoshida, in: T. Narita, T. Maruyama, S. Taniguchi (Eds.), International Symposium on High Temperature Corrosion and Protection 2000, Science Reviews, Hokkaido, 2000, p. 443.

- [3] J.L. Blough, G.J. Stanko, in: J.F. Norton, N.J. Simms, W.T. Bakker, I.G. Wright (Eds.), *Materials Performance in Waste to Energy Plants, Life Cycle Issues in Advanced Energy Systems*, Science Reviews, Woburn, UK, 2002, p. 195.
- [4] M. Montgomery, A. Karlsson, *Mater. Corros.* 50 (1999) 579.
- [5] H.P. Nielsen, L.L. Baxter, G. Sclippab, C. Morey, F.J. Frandson, K. Dam-Johansen, *Fuel* 79 (2000) 131.
- [6] M. Noguchi, K. Matsuoaka, H. Sakamoto, U. Shigeki, Y. Sawada, *Mater. Sci. Forum* 522–523 (2006) 555.
- [7] A. Sato, H. Takahashi, M. Yoshiba, *Mater. Sci. Forum* 522–523 (2006) 87.
- [8] www.pvcplus.net, 2014.
- [9] E.A. Brandes, G.B. Brook (Eds.), *Smithells Metals Reference Book*, Butterworth-Heinemann, UK, 1992.
- [10] B. Downey, J. Bermel, P. Zimmer, *Corrosion* 25 (1969) 502.
- [11] G. Heinemann, F. Harrison, P. Haber, *Ind. Eng. Chem.* 38 (1946) 496.
- [12] G. Tammann, *Z. Anorg. Allg. Chem.* 111 (1920) 78.
- [13] S.I. Ali, A. Moccari, *Br. Corros. J.* 14 (1978) 142.
- [14] K. Hauffe, J. Hinrichs, *Werkst. Korros.* 21 (1970) 954.
- [15] D.W. McKee, D.W. Shores, K.L. Luthra, *J. Electrochem. Soc.* 125 (1979) 411.
- [16] M.J. McNallan, W.W. Liang, S.H. Kim, C.T. Kang, in: R.A. Rapp (Ed.), *High Temperature Corrosion*, NACE, Houston, TX, 1983, p. 316.
- [17] M.J. McNallan, W.W. Liang, J.M. Oh, C.T. Kong, *Oxid. Met.* 17 (1982) 371.
- [18] H. Latreche, S. Doublet, M. Schutze, *Oxid. Met.* 72 (2009) 1.
- [19] H. Latreche, S. Doublet, M. Schutze, *Oxid. Met.* 72 (2009) 31.
- [20] J.M. Oh, M.J. McNallan, G.Y. Lai, M.F. Rothman, *Met. Trans. A* 17A (1986) 1087.
- [21] Y.-K. Li, R.A. Rapp, *Met. Trans. B* 14B (1983) 509.
- [22] B.B. Ebbinghaus, *Combust. Flame* 101 (1995) 311.
- [23] C. Schwalm, M. Schutze, *Mater. Corros.* 51 (2000) 161.
- [24] Y. Ihari, H. Ohgame, K. Sakiyama, K. Hashimoto, *Corros. Sci.* 21 (1981) 805.
- [25] Y. Ihara, H. Ohgame, K. Sakiyama, K. Hashimoto, *Corros. Sci.* 22 (1982) 901.
- [26] Y. Ihara, H. Ohgame, K. Sakiyama, K. Hashimoto, *Corros. Sci.* 23 (1983) 167.
- [27] D. Bramhoff, H.J. Grabke, H.P. Schmidt, *Mater. Corros.* 40 (1989) 643.
- [28] J.-M. Abels, H.-H. Strehblow, *Corros. Sci.* 39 (1996) 115.
- [29] O. Kubaschewski, C.B. Alcock, P.J. Spencer, *Materials Thermochemistry*, sixth ed., Pergamon Press, Oxford, 1993.
- [30] A. Zahs, M. Spiegel, H.J. Grabke, *Corros. Sci.* 42 (2000) 1093.
- [31] R. Prescott, F.H. Stott, P. Elliott, *Oxid. Met.* 31 (1989) 145.
- [32] F.H. Stott, R. Prescott, P. Elliot, *Mater. Sci. Technol.* 6 (1990) 364.
- [33] Y. Sato, D.J. Young, *Oxid. Met.* 55 (2001) 243.
- [34] Y. Sato, D.J. Young, in: T. Narita, T. Maruyama, S. Taneguchi (Eds.), *High Temperature Corrosion and Protection 2000*, Science Reviews, Northwood, 2000, p. 119.
- [35] P. Elliot, G. Marsh, *Corros. Sci.* 29 (1984) 703.
- [36] M.F. Rothman, G.Y. Lai, D.E. Fluck, Paper No. 17, in: *Corrosion 85*, NACE, 1985.
- [37] M. Sanchez Pasten, M. Spiegel, *Mater. Corros.* 57 (2006) 192.
- [38] D. Bruce, P. Hancock, *J. Inst. Met.* 97 (1969) 140.
- [39] P. Hancock, R.C. Hurst, A.R. Sollarg, *Chemical Metallurgy of Iron and Steel*, Iron and Steel Institute, London, 1973, p. 415.
- [40] E. Reese, H.J. Grabke, *Mater. Corros.* 43 (1992) 547.
- [41] E. Reese, H.J. Grabke, *Mater. Corros.* 44 (1993) 41.

- [42] Y. Shinata, *Oxid. Met.* 27 (1987) 315.
- [43] Y. Shu, F. Wang, W. Wu, *Oxid. Met.* 51 (1999) 97.
- [44] J. Pettersson, H. Asteman, J.-E. Svensson, L.-G. Johansson, *Oxid. Met.* 64 (2005) 23.
- [45] J. Pettersson, J.-E. Svensson, L.-G. Johansson, *Oxid. Met.* 72 (2009) 159.
- [46] C. Proff, T. Jonsson, C. Pettersson, J.-E. Svensson, L.-G. Johansson, M. Halvarsson, in: G.J. Tatlock, H.E. Evans (Eds.), *Microscopy of Oxidation*, Science Reviews, 2008, p. 93.
- [47] H.J. Grabke, E. Reese, M. Spiegel, *Corros. Sci.* 37 (1995) 1023.
- [48] M. Spiegel, *Mater. High Temp.* 14 (1997) 221.
- [49] M. Montgomery, A. Karlsson, A. Larssen, *Mater. Corros.* 53 (2002) 121.
- [50] P. Viklund, A. Kjornhede, P. Henderson, A. Stalenheim, R. Pettersson, *Fuel Proc. Technol.* 105 (2013) 106.
- [51] H.H. Krause, D.A. Vaughan, W.K. Boyd, *Trans. ASME J. Eng. Power* A97 (1975) 448.
- [52] H. Kassman, J. Pettersson, B.-M. Steenari, L.-E. Amand, *Fuel Proc. Technol.* 105 (2013) 170.
- [53] H.H. Krause, in: M.F. Rothman (Ed.), *High Temperature Corrosion in Energy Systems*, Metallurgical Society AIME, 1985, p. 83.
- [54] M. Montgomery, T. Vilhelmsen, S.A. Jensen, *Mater. Corros.* 59 (2008) 783.
- [55] L.S. Johanson, B. Leckner, L.-E. Amand, K. Davidson, *Energy Fuels* 22 (2008) 3005.
- [56] J. Silvennoinen, M. Hedman, *Fuel Proc. Technol.* 105 (2013) 11.
- [57] S.C. Okoro, M. Montgomery, F.J. Frandsen, K. Pantleon, *Mater. High Temp.* 32 (2015) 92.
- [58] P. Kilgallon, N.J. Simms, J.E. Oakey, Paper No. 05318, in: *Corrosion 2005*, NACE International, 2005.
- [59] E.C. Zabetti, V. Barisic, B. Moulton, in: 34th International Technical Conference on Coal Utilisation and Combustion, Coal Technology Association, Clearwater, FL, 2009.
- [60] S. Enestam, J. Niemi, K. Makela, in: 33rd International Conference on Clean Coal and Fuel Systems, Coal Technology Association, Clearwater, FL, 2010.
- [61] R. Elger, F. Lindberg, R. Norling, R. Pettersson, *Mater. High Temp.* 32 (2015) 36.
- [62] H. Hooshyar, J. Liske, L.-G. Johansson, M. Seemann, T. Jonsson, *Mater. High Temp.* 32 (2015) 197.
- [63] N. Israelsson, J. Engkvist, K. Hellstrom, M. Halvarsson, J.-E. Svensson, L.-G. Johansson, *Oxid. Met.* 83 (2015) 29.
- [64] N. Israelsson, K. Hellstrom, J.-E. Svensson, L.-G. Johansson, *Oxid. Met.* 83 (2015) 1.
- [65] Q. Peng, X. Wei, J. Ding, J. Yang, X. Yang, *Int. J. Energy Res.* 32 (2008) 1164.
- [66] J.G. Cordaro, N.C. Rubin, R.W. Bradshaw, *J. Solar Energy* 133 (2011), 011014.
- [67] L.C. Olsen, J.W. Ambrosek, K. Sridharan, M.H. Anderson, T.R. Allen, *J. Fluorine Chem.* 130 (2009) 67.
- [68] G.J. Janz, C.B. Allen, J.R. Downey, R.P.T. Tomkins, Physical properties data compilations relevant to energy storage 1. Molten salts: eutectic data <http://www.nist.gov/data/nslrds/NSRDS-NBS-61-1>.
- [69] J.E. Indacochea, J.L. Smith, K.R. Litko, E.J. Karell, *J. Mater. Res.* 14 (1999) 1990.
- [70] J.E. Indacochea, J.L. Smith, K.R. Litko, E.J. Karell, A.G. Raraz, *Oxid. Met.* 55 (2001) 1.
- [71] F. Mansfield, N.E. Paton, W.M. Robertson, *Met. Trans. B* 4 (1972) 321.
- [72] C. Edeleanu, R. Littlewood, *Electrochim. Acta* 3 (1960) 195.
- [73] R. Combes, J. Vedel, B. Tremillion, *Electrochim. Acta* 20 (1975) 191.
- [74] T. Ishitsuka, K. Nose, *Mater. Corros.* 51 (2000) 177.
- [75] M. Takahashi, *Molten Salts* 37 (1994) 215.
- [76] Y. Kawahara, M. Nakamura, H. Tsuboi, K. Yukawa, Paper No. 165, in: *Corrosion 97*, NACE International, 1997.
- [77] Y. Kawahara, *Corros. Sci.* 44 (2002) 223.

- [78] M. Spiegel, A. Zaha, H.J. Grabke, Life Cycle Issues in Advanced Energy Systems, Science Reviews, 2003.
- [79] <http://www.crct.polymtl.ca/fact/documentation/FTsalt/KCl-ZnCl2.jpg>.
- [80] A. Ruh, M. Spiegel, Corros. Sci. 48 (2006) 679.
- [81] Y.S. Li, Y. Niu, W.T. Wu, Mater. Sci. Eng. A 345 (2003) 64.
- [82] M. Spiegel, Molten Salt Forum 7 (2003) 253.
- [83] D. Orlicka, N.J. Simms, T. Hussain, J.R. Nicholls, Mater. High Temp. 32 (2015) 167.
- [84] R. Olivares, Solar Energy 86 (2012) 2576.
- [85] Y. Wu, N. Ren, T. Wang, C. Ma, Solar Energy 85 (2011) 1957.
- [86] G. Sirotkin, Russ. J. Inorg. Chem. 4 (1959) 1180.
- [87] G.S. Picard, T. Flament, B.L. Tremillon, J. Electrochem. Soc. 132 (1985) 863.
- [88] G.S. Picard, H.M. Lefebvre, B.L. Tremillon, J. Electrochem. Soc. 134 (1987) 52.
- [89] A.J. Arvia, J.J. Podesta, R.C. Piatti, Electrochim. Acta 16 (1971) 1797.
- [90] I.B. Singh, U. Sen, Corros. Sci. 34 (1993) 1733.
- [91] S.H. Goodes, R.W. Bradshaw, J. Mater. Eng. Perform. 2004 (2004) 78.
- [92] I.B. Singh, G. Venkatachari, K. Balakrishnan, Corros. Sci. 36 (1994) 1777.
- [93] A. Fernandez, M. Losanta, F.J. Perez, Oxid. Met. 78 (2012) 329.
- [94] A.G. Fernandez, H. Galleguillos, F.J. Perez, Oxid. Met. 82 (2014) 331.
- [95] C. Yuh, A. Hilmi, L. Chen, A. Franco, M. Farooque, ECS Trans. 41 (2012) 21.
- [96] C.E. Baumgartner, J. Electrochem. Soc. 67 (1984) 1850.
- [97] M.L. Orfield, D.A. Shores, J. Electrochem. Soc. 135 (1988) 1662.
- [98] M.L. Orfield, D.A. Shores, J. Electrochem. Soc. 136 (1992) 2862.
- [99] K. Ota, S. Asano, H. Yoshitaka, N. Kamiya, J. Electrochem. Soc. 139 (1992) 667.
- [100] K. Matsuzawa, T. Mizusaki, S. Mitsushima, N. Kamiya, K. Ota, J. Power Sources 140 (2005) 258.
- [101] K. Matsuzawa, G. Tatezawa, Y. Matsuda, S. Mitsushima, N. Kamiya, K. Ota, J. Electrochem. Soc. 152 (2005) A1116.
- [102] A. Melendez-Caballeros, V. Albin, S.M. Fernandez-Valverde, Electrochim. Acta 140 (2014) 174.
- [103] H.S. Hsu, J.H. DeVan, M. Howell, J. Electrochem. Soc. 134 (1987) 3038.
- [104] M. Spiegel, P. Biedenkopf, H.J. Grabke, Corros. Sci. 39 (1997) 1193.
- [105] R.E. Andresen, J. Electrochem. Soc. 126 (1979) 328.
- [106] T. Nishina, I. Uchida, J.R. Selman, J. Electrochem. Soc. 141 (1994) 1191.
- [107] H.S. Hsu, J.H. DeVan, J. Electrochem. Soc. 133 (1986) 2077.
- [108] D.A. Shores, P. Singh, Proc. Electrochem. Soc. 84 (1984) 271.
- [109] F.J. Perez, M.P. Hierro, D. Duday, C. Gomez, M. Romero, L. Daza, Oxid. Met. 53 (2000) 375.
- [110] C.L. Zeng, Y. Liu, High Temp. Mater. Proc. 30 (2011) 161.
- [111] S. Ahn, K. Oh, M. Kim, Int. J. Hydrogen Energy 39 (2014) 12291.
- [112] W.B.A. Sharp, D.L. Singbeil, J.R. Keiser, in: Corrosion 2012, NACE International, 2012, p. 1308.
- [113] M.C. Galetz, J.T. Bauer, M. Schuetze, M. Noguchi, H. Cho, J. Therm. Spray Technol. 22 (2013) 828.
- [114] M. Usitalo, P.M. Vuorista, T. Mantyla, Corros. Sci. 46 (2004) 1311.
- [115] P.Y. Guo, C.L. Zeng, N. Wang, Y. Shao, J. Power Sources 217 (2012) 485.
- [116] C. Ni, L.Y. Lu, C.L. Zeng, Y. Niu, J. Power Sources 261 (2014) 162.
- [117] M.C. Galetz, B. Rammer, M. Schuetze, Oxid. Met. 81 (2014) 151.
- [118] H.-E. Zschau, M. Schuetze, Mater. Sci. Forum 696 (2010) 366.
- [119] A. Donchev, B. Gleeson, M. Schuetze, Intermetallics 11 (2003) 387.
- [120] H.-E. Zschau, V. Gauthier, G. Schumacher, F. Dettenwanger, M. Schuetze, H. Baumann, K. Bethge, M. Graham, Oxid. Met. 59 (2003) 183.